AGU PUBLICATIONS

JGR

Journal of Geophysical Research: Oceans

RESEARCH ARTICLE

10.1002/2016JC012294

Intrusive upwelling in the Central Great Barrier Reef

Jessica A. Benthuysen[1], Hemerson Tonin[1], Richard Brinkman[1], Michael Herzfeld[2], and Craig Steinberg[1]

[1]Australian Institute of Marine Science, Townsville, Australia, [2]CSIRO Oceans and Atmosphere, Hobart, Australia

Key Points:
- A metric is used to identify intrusive upwelling from 6 years of mooring data in Palm Passage
- A hydrodynamic model reveals widespread cooling along the seafloor, concentrated in reef passages
- Along-shelf wind fluctuations control the shelf currents and the timing of intrusive upwelling

Correspondence to:
J. Benthuysen,
j.benthuysen@aims.gov.au

Citation:
Benthuysen, J. A., H. Tonin, R. Brinkman, M. Herzfeld, and C. Steinberg (2016), Intrusive upwelling in the Central Great Barrier Reef, *J. Geophys. Res. Oceans*, *121*, 8395–8416, doi:10.1002/2016JC012294.

Received 30 AUG 2016
Accepted 8 NOV 2016
Accepted article online 11 NOV 2016
Published online 30 NOV 2016

Abstract In the Central Great Barrier Reef, the outer continental shelf has an open reef matrix that facilitates the exchange of waters with the Coral Sea. During austral summer, cool water intrudes onto the shelf along the seafloor. Temperature observations reveal cool, bottom intrusions during a 6 year period from the Queensland Integrated Marine Observing System's Palm Passage mooring. A metric is used to identify 64 intrusion events. These intrusions predominantly occur from October to March including the wet season. During an event, the outer-shelf's near-bottom temperature decreases by 1–3°C typically over 1 week. The near-bottom salinity tends to increase, while near-surface changes do not reflect these tendencies. Intrusion events occur predominantly with either weakening equatorward winds or poleward wind bursts. A regional hydrodynamic model for the Great Barrier Reef captures the timing and amplitude of these intrusions. During intrusion events, isotherms tend to uplift over the continental slope and onto the shelf and the East Australian Current intensifies poleward. Over the shelf, a bottom-intensified onshore current coincides with bottom cooling. For numerous events, the model diagnostics reveal that the cross-shelf flow is dominated by the geostrophic contribution. A vertical circulation tilts the isopycnals upward on the southern side of the passage, causing an along-shelf density gradient and geostrophic onshore flow with depth. While wind fluctuations play a major role in controlling the along-shelf currents, model results indicate that a concurrent topographically induced circulation can assist the onshore spread of cool water.

1. Introduction

The Central Great Barrier Reef (GBR) (16–20°S) has an open reef matrix along the outer-shelf compared to the north and south. There are channels, such as Palm Passage, which facilitate the exchange of water between the shelf and the Coral Sea. During austral summer, cool water is uplifted over the slope and flows onto the shelf along the seafloor [*Andrews and Furnas*, 1986]. These periods of bottom cooling are termed "intrusions" as they are not reflected in the surface temperature [*Rochford*, 1991]. The first records of intrusions of Coral Sea water onto the Central GBR's continental shelf date back to the British Museum Expedition in the 1920s [*Orr*, 1933]. Since then studies have aimed to describe their physical characteristics and driving mechanisms.

These intrusions are important by influencing the thermal structure of waters over the shelf. The near-bottom cooling can potentially provide relief for the shelf's benthic marine ecosystems from the impacts of strong summertime warming [*Glynn*, 1996; *Riegl and Piller*, 2003; *Bongaerts et al*., 2010] and marine heat waves [*Hobday et al*., 2016; *Steinberg*, 2007]. They can impact a wide portion of the shelf by occurring coherently over hundreds of kilometers alongshore [*Andrews and Furnas*, 1986]. Intrusion events can spread onshore by incursions of 50 km over 1 week or 100 km over several weeks [*Andrews and Furnas*, 1986] and can reach near-shore reef communities [*Berkelmans et al*., 2010]. Intrusions are estimated to propagate onshore at speeds of 10–60 cm s^{-1} [*Andrews and Furnas*, 1986].

The intrusions induce cross-shelf changes in nutrient supply for reef communities from the shelf-edge to the lagoon [*Andrews and Gentien*, 1982; *Andrews*, 1983a]. The upwelled water entrains nutrients and provides an important source for the Central GBR continental shelf [*Furnas and Mitchell*, 1996]. Nutrient input can enhance biological productivity evidenced by high chlorophyll patches on the outer-shelf during the wet season [*Andrews and Gentien*, 1982; *Furnas and Mitchell*, 1996]. The intrusions are associated with uplift of cool, high saline, low oxygen, and nitrate rich water estimated from 125 m depth offshore [*Andrews and Gentien*, 1982].

© 2016. American Geophysical Union. All Rights Reserved.

Past studies have identified physical mechanisms driving intrusions onto the shelf. Internal waves, such as internal tides, raise subthermocline water at the shelf edge [*Wolanski and Pickard*, 1983] but tidal excursions may be limited to the outer-shelf [*Andrews and Furnas*, 1986]. Along-shelf wind fluctuations can modulate the along-shelf flow on timescales of less than a day and induce changes on seasonal timescales [*Burrage et al*., 1991]. The winds are characterized by southeasterly trade winds from April to October and are more variable, including poleward winds, during the summer monsoon [*Wolanski*, 1994]. Poleward flow can induce an onshore bottom Ekman transport advecting cooler water onshore [*Andrews and Gentien*, 1982; *Andrews*, 1983b]. Time series from 1980 to 1983 at Rib Reef, in Palm Passage, revealed large intrusion events associated with poleward wind bursts and onshore currents near the bottom [Figure 5 in *Andrews and Gentien*, 1982; Figure 2 in *Andrews and Furnas*, 1986].

Furthermore, the poleward flowing East Australian Current (EAC) fluctuates with a 90–120 day period over the continental slope [*Andrews and Gentien*, 1982; *Andrews and Furnas*, 1986]. As the EAC intensifies poleward, cooler water rises upward over the slope and possibly on the shelf and sets the source waters of the intrusions [*Andrews and Gentien*, 1982]. The EAC strengthening (weakening) is associated with isopycnals tilting upward (downward) over the slope [*Steinberg*, 2007]. However, boundary current uplift alone may penetrate only 5–10 km onto the shelf [*Garrett*, 1979]. Hence, the role of wind fluctuations over the shelf is important to understand in driving the intrusions onshore.

The objectives of this work are to characterize cool, salty bottom intrusions in the Central GBR, including their seasonal occurrence, the intensity of bottom cooling and duration. This study aims to identify mechanisms responsible for the bottom currents causing intrusions and cross-shelf exchange from the slope onto the shelf. Intrusions are identified in mooring observations at Palm Passage and linked to fluctuations in the winds and source waters over the slope. A complementary analysis using a regional hydrodynamic model further elucidates the roles of winds and the density field in forcing the shelf circulation during intrusion events.

The paper is outlined as follows. In section 2, the mooring, wind, and model data and analysis methods are described, and a bottom intrusion index is defined. Section 3 presents the characteristics of intrusions over the shelf from observations and the analyses of offshore source waters and the role of wind forcing during intrusions. Section 4 compares the observations with the hydrodynamic model results and presents analyses of the source waters, links with the EAC, and wind-driven and density-driven circulation over the shelf. Finally, sections 5 and 6 present the discussions and conclusions.

2. Data and Methods

2.1. Observational Data

In the Central GBR, the Queensland node of the Integrated Marine Observing System manages the deployment of the moorings in Palm Passage (PPS; outer-shelf, ~70 m isobath; 18.31°S, 147.16°E) and at Myrmidon Reef (MYR; continental slope, ~205 m isobath; 18.22°S, 147.34°E) (Figure 1). The Palm Passage mooring deployments commenced in November 2008, and the Myrmidon Reef mooring deployment commenced in October 2007. Six years of data are analyzed from June 2009 to mid-May 2015.

At Palm Passage, the mooring includes a bottom-mounted ADCP that measures the current velocity in 2 m bins at 10 min intervals. The depth-averaged velocity is calculated following a similar method in *Shearman and Lentz* [2003] and *Schaeffer et al*. [2013], and the velocity is assumed constant from 10 m depth to the surface and constant below the lowest measurement. The water temperature is measured through the water column with Seabird temperature sensors located at 8–30 m intervals. From June 2013 to May 2015, there are six temperature sensors spaced 8–10 m intervals. The temperature data are recorded every 1, 5, or 10 min and are quality controlled through the IMOS toolbox. Temporal gaps in the measurements were not included in the analysis. From 7 June 2009 to 20 May 2015, the temperature data from 15 to 60 m depth had a temporal coverage of 93%. Salinity data are available from WETLABS water quality meters (WQMs) near-surface (11–17 m depth) and near-bottom (~56 m depth and 12 m above bottom prior to June 2013 and ~70 m depth and 0.5 m above bottom afterward). The near-surface (near-bottom) salinity data had a temporal coverage of 67% (60%) over the full time period. Near-surface salinity had 92% coverage from 19 April 2011 to 10 April 2015. The ADCP velocity data had a temporal coverage of 88%. To examine the

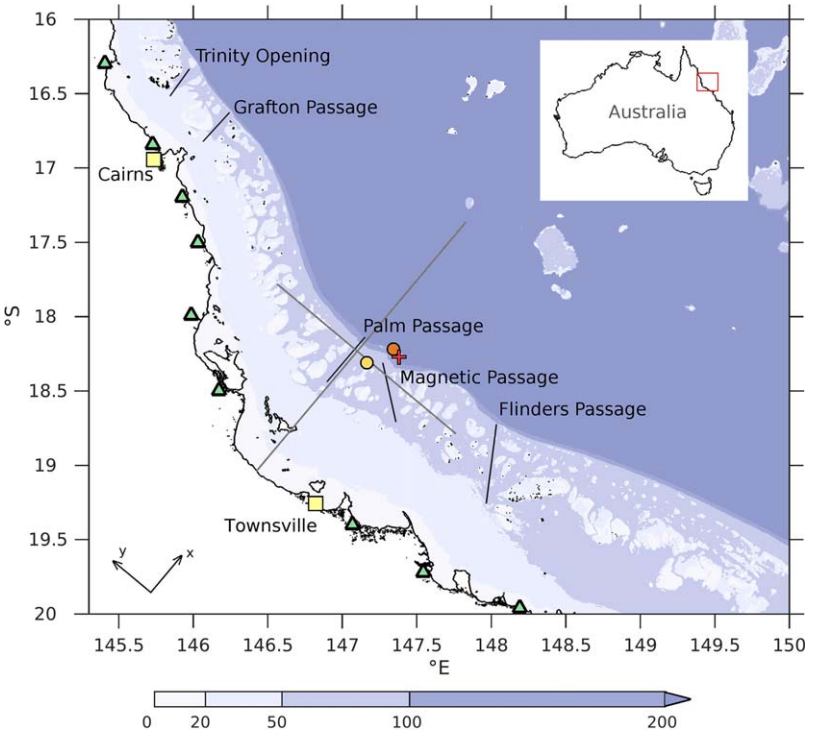

Figure 1. Central Great Barrier Reef map and bathymetry (m) from gbr100. The plotted symbols correspond to moorings at PPS (yellow circle) and MYR (orange circle) and the Myrmidon Reef weather station (red cross). The along-shelf and cross-shelf coordinates are indicated in the lower left corner. The transects plotted through Palm Passage are indicated by the grey lines. The green triangles indicate the river locations from the model corresponding to the north to south: Daintree, Barron, Mulgrave and Russell, Johnstone, Tully, Herbert, Haughton, Burdekin, and Don rivers.

subinertial variability, the time series for temperature and currents are averaged onto hourly intervals and low-pass filtered using the PL64 filter with a 38 h half power period [*Rosenfeld*, 1983].

From the Myrmidon Reef mooring, temperature is analyzed near the bottom (2–5 m above the bottom) and at ~95 m depth (ranging from 90 to 100 m). The temperature data are recorded every 5 min from Seabird temperature sensors. Over the 6 year time period, the temperature at 200 m (95 m) had a temporal coverage of 80% (64%). Most of the temporal gap occurred from November 2013 to November 2014 when no mooring was present.

Wind observations were obtained from the Myrmidon Reef weather station (18.27°S, 147.38°E) using the 30 min data at 10 m height above the surface from June 2009 to January 2011. The wind stress is calculated following *Gill* [1982] and low-pass filtered as above. Hourly wind stress data are also obtained from the regional version of the Australian Community Climate and Earth-System Simulation (ACCESS-R; 12 km resolution) [*Bureau of Meteorology*, 2010] from August 2010 to June 2015. During overlapping time periods, the wind stress shows good agreement with a skill score (equation (2)) of 0.92 from 8 August 2010 to 1 February 2011. After Cyclone Yasi, a temporary buoy with weather sensors was placed at Myrmidon Reef. Calculated wind stress without correcting for height continues to show agreement with the ACCESS-R wind stress. However, the time series includes periods without data. Hence, the Myrmidon Reef weather station data are used only from June 2009 to July 2010 and ACCESS-R winds are used from August 2010 to June 2015 in the analysis.

2.2. eReefs Hydrodynamic Model

The eReefs project is designed to investigate currents and water quality for the whole of the GBR [e.g., *Schiller et al*., 2014]. The hydrodynamic model uses the Sparse Hydrodynamic Ocean Code (SHOC) [*Herzfeld*, 2006; *Herzfeld et al*., 2008], which is a three-dimensional, finite-difference Arakawa C-grid model that uses the hydrostatic and Boussinesq assumptions. The curvilinear orthogonal, horizontal grid is ~4 km resolution, extending from the New South Wales/Queensland border to Papua New Guinea, and has a

domain width of 380 km (south) to 640 km (north). The vertical grid extends to 4000 m depth, with 1 m resolution near the surface to 200 m near the bottom in the deep ocean. Partial cells are used to represent bottom topography. Bathymetry is sourced from the digital elevation model of the GBR at 100 m spatial resolution (gbr100) [*Beaman*, 2010]. The model time step is typically 90 s and reduced when necessary.

The surface forcing of momentum, heat, and freshwater fluxes is derived from ACCESS-R. At the oceanic open boundaries, the model is forced by OceanMAPS, the Bureau of Meteorology's operational ocean prediction system (~10 km horizontal resolution around Australia) developed from the BLUElink project [*Oke et al*., 2008]. Tides are implemented [*Eanes and Bettadpur*, 1995; *Herzfeld and Andrewartha*, 2012] from a global tidal model [*Cartwright and Ray*, 1990]. River flows input into the model are from the Queensland Department of Natural Resources and Mines stream gauging station network.

The Smagorinsky scheme is applied for horizontal mixing, and the κ–ε turbulence closure scheme is applied for the vertical mixing parameterization. A quadratic bottom drag law is used with a typical quadratic drag coefficient 2.5×10^{-3}. Additional information on the model configuration and model validation is provided in *Herzfeld et al*. [2013], *Herzfeld et al*. [2014], and *Schiller et al*. [2015]. The model is not run in data-assimilation mode and hence the model is free-running and dynamically consistent. The model is run from mid-September 2010 to June 2015.

2.3. Data Processing and Metrics

The currents are oriented in an along- and cross-shore coordinate system where the *x* axis is positive offshore and the *y* axis is positive equatorward. Following *Burrage et al*. [1991], the along-shelf direction is rotated 310° relative to true north (Figure 1), defined by large-scale shelf topography. Principal component directions were calculated from the depth-averaged subinertial velocity at PPS and ACCESS-R winds using the formula in *Kundu and Allen* [1976]. From 310°T, the principal component direction departed 3°W (from PPS velocity data) and 2°E (from Myrmidon Reef wind data), which is within the range of directions found in historic nearby wind data and shelf and slope moorings [*Burrage et al*., 1991].

Cool bottom intrusions are identified from the Palm Passage mooring in two steps. First, the near-surface and near-bottom temperature, T_s and T_b, respectively, are low-pass filtered. Cooling periods are determined when T_b decreases for more than a day. In order to neglect small rises in temperature separating adjacent periods, the cooling period may be extended if separated by less than 3 days. The periods are joined if: the second period's initial T_b is less than the first period's initial T_b and if the second period's final T_b is less than the first period's final T_b. Second, a metric is defined to distinguish intrusion events from other periods when the near-bottom temperature decreases. A bottom intrusion index, I, is calculated for each period when T_b decreases:

$$I = \frac{|\Delta T_b|}{\bar{T}_b} \times \frac{(\bar{T}_s - \bar{T}_b)}{(\bar{T}_s + \bar{T}_b)/2} \times 1000 \tag{1}$$

where ΔT_b is the change in T_b and the overbars signify the time-mean quantity over that period. The first term is a nondimensional measure of the intensity of cooling, and the second term is a simple nondimensional measure of the stratification based on near-surface and near-bottom temperatures. These two terms are multiplied since both contributions need to be present during an intrusion. This quantity is multiplied by a factor of 1000 so that values range from 0 to 100. The index increases for increasingly significant intrusions, i.e., when there is a notable decrease in T_b while stratification is present. A threshold value is determined based on cooling periods during the autumn/wintertime breakdown of the stratification (Figure 2). During this time period, a decrease in temperature occurs near the surface and bottom, and in the index I, this decrease is counteracted by weak stratification. From the intrusion indices during this time period, a threshold value of "2" is applied in order to exclude this cooling period and smaller intrusions predominantly in winter. The main intrusions events occur when $I > 2$ in the Palm Passage mooring's temperature time series. Similarly, the near-surface and near-bottom salinity are defined as S_s and S_b, respectively.

To compare the eReefs model output with the mooring results, the near-bottom temperature was assessed using the skill score [*Willmott*, 1981; *Warner et al*., 2005]. The skill score is defined as

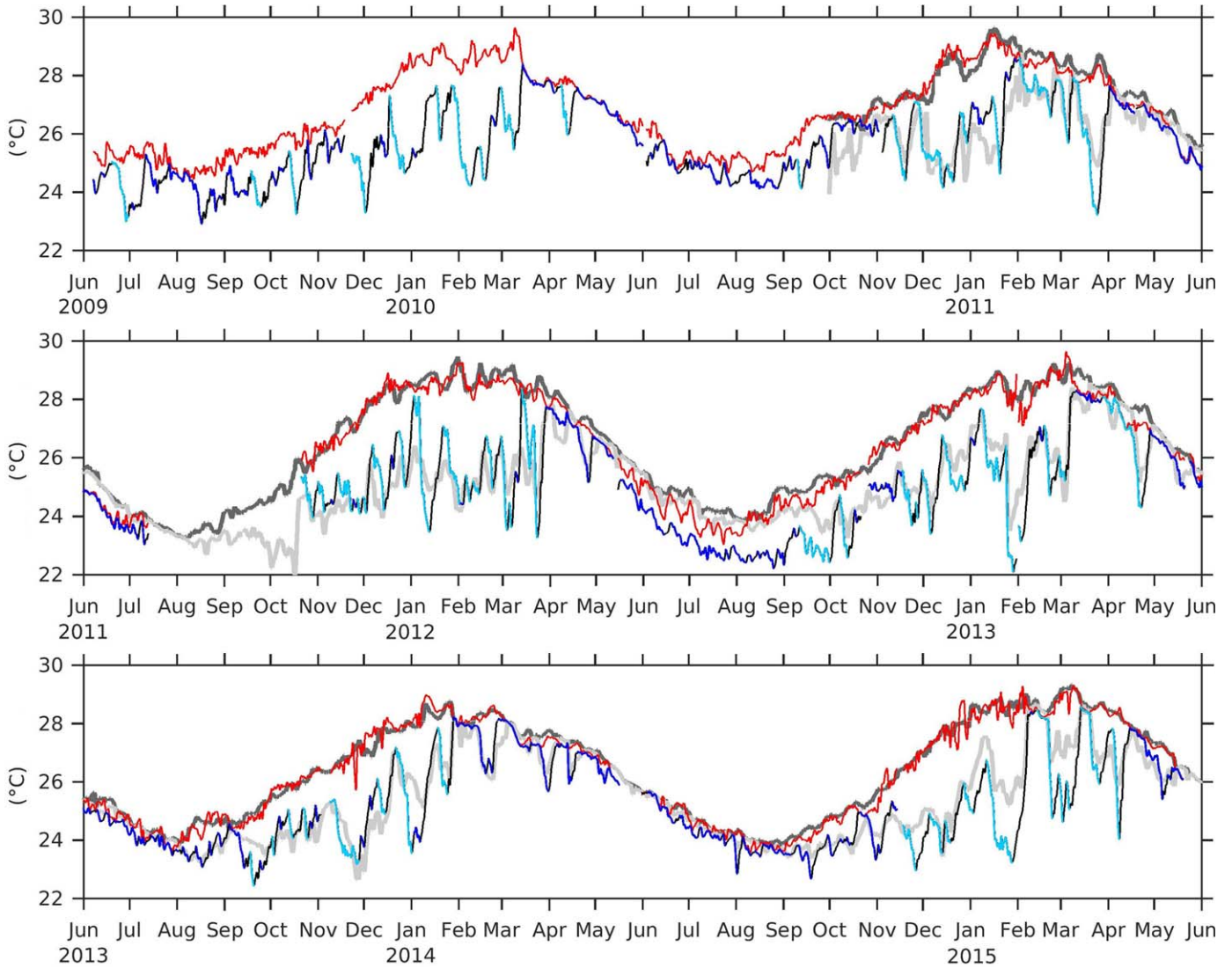

Figure 2. Near-surface and near-bottom temperature from the Palm Passage mooring and the eReefs model. The time series are for (top) June 2009–2011, (middle) June 2011–2013, and (bottom) June 2013–2015. From the mooring, T_s (thin red curve) and T_b (thin curves that are black when increasing and blue when decreasing) are plotted. The light blue curves indicate intrusion events ($I > 2$). From the model, T_s (thick dark grey curve) and T_b (thick light grey curve) are plotted.

$$Skill = 1 - \frac{\sum |X_{model} - X_{obs}|^2}{\sum \left(|X_{model} - \bar{X}_{obs}| + |X_{obs} - \bar{X}_{obs}|\right)^2}, \quad (2)$$

where X is the quantity for comparison, $\bar{X}$ is the time mean quantity for each period, and *model* and *obs* denote the model results and observations, respectively. The skill score is 1.0 when the model perfectly agrees with observations and 0 when there is complete disagreement. In order to determine the dynamics underpinning intrusive upwelling in the observations, events in the model are investigated when $Skill > 0.6$ for T_b during an intrusion event.

3. Observations: Characteristics of Bottom Intrusions

3.1. Seasonality

Over the shelf, the waters at the Palm Passage mooring exhibit a seasonal cycle of near-surface warming during austral summer followed by a breakdown in stratification and cooling throughout the water column during winter (Figure 2). From October to April, episodic cooling events occur near the bottom, occasionally spanning a substantial portion of the water column. These cooling events are not necessarily reflected in

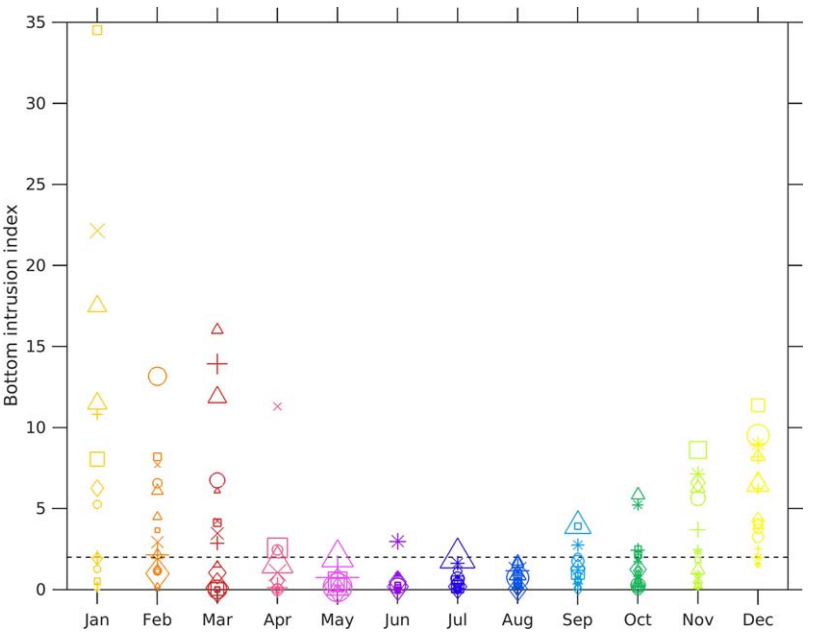

Figure 3. The seasonal occurrence of all bottom cooling periods and their corresponding bottom intrusion index. The years plotted are 2009 (*), 2010 (o), 2011 (+), 2012 (triangle), 2013 (square), 2014 (diamond), and 2015 (×). The colors indicate the month when the cooling period occurs. The size of the symbols represent the period duration, ranging from 1 day (smallest) to 73 days (largest, May 2011). The dashed line indicates the threshold value of I = 2.

the near-surface temperature, which may continue warming despite cooling below. To examine these intrusions, the temperature at 15 m (T_s) and 60 m (T_b) is plotted in time (Figure 2), and cooling periods are identified and bottom intrusion indices are calculated for each period.

Over the 6 years, there are 188 periods when T_b decreases by using the method describe in section 2. Of these occurrences, 64 periods are classified as intrusion events. The seasonal occurrence for intrusions shows they predominantly occur during austral summer (Figure 3). Of the 64 intrusion events, 56 events, i.e., 88%, occur between October and March. From October to March, the number of intrusion events (and days of near-bottom cooling) are the following: 2009–2010: 7 (50 days), 2010–2011: 8 (84 days), 2011–2012: 15 (82 days), 2012–2013: 10 (58 days), 2013–2014: 7 (47 days), and 2014–2015: 7 (69 days). Smaller scale events, with $I < 2$, may contribute to the number of upwelling days but are not considered here. On average, there are 1–2 intrusion events per month between October and March, with the highest number of occurrences in December.

3.2. Near-Bottom Temperature and Salinity

During intrusion events at PPS, T_b undergoes cooling and temperature decreases are significantly greater than changes in T_s (Figures 2 and 4a, and 4c). T_s tends to increase during an event, which may reflect that intrusions occur during summertime warming. During events in February and March, T_s tends to increase despite occurring after the peak in summertime warming. The mean ΔT_s and standard deviation are 0.2 ± 0.4°C from the 64 intrusion events. In contrast, the mean ΔT_b and standard deviation are -2.0 ± 1.1°C. Excluding April with several events that co-occur with stratification breakdown, the greatest mean decrease in T_b (-3.1°C) occurs in January. The maximum decrease in T_b recorded is -5.1°C in March 2012 with $I = 12$.

Meanwhile, near-bottom cooling coincides with increasing salinity. Of the 44 intrusion events in which near-bottom salinity data are present, the mean ΔS_b and standard deviation are 0.23 ± 0.16°C. The change in near-bottom temperature and salinity tends to follow a linear relationship (Figure 4c).The near-bottom changes in salinity are not reflected in near-surface changes (Figures 4a and 4c). The event with the maximum decrease in T_b in March 2012 corresponds with one of the greatest increases in S_b (+0.55 psu) and the greatest freshening in S_s (-0.82 psu). At the outer-shelf, the near-surface and near-bottom T/S characteristics are significantly different during the peak of the intrusion (Figures 4b and 4d) reflecting different

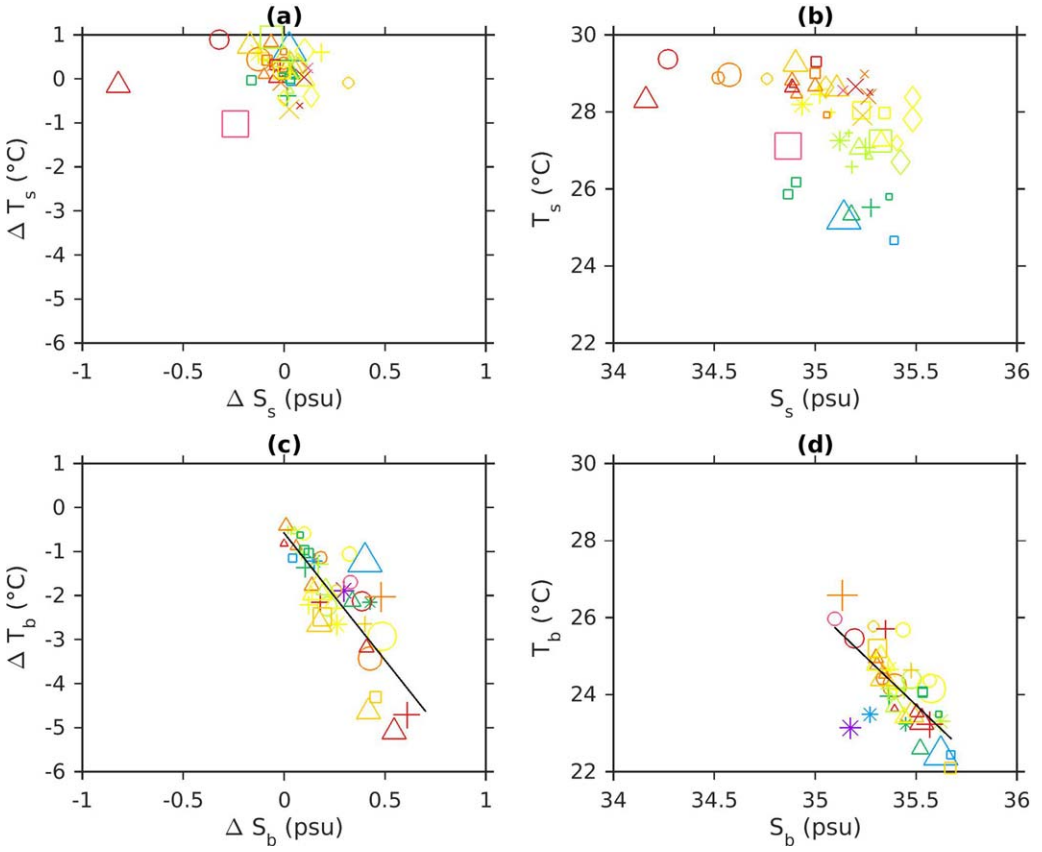

Figure 4. Over the bottom cooling period at PPS, the change in (a) near-surface and (c) near-bottom salinity are plotted against the corresponding change in temperature. The (b) near-surface and (d) near-bottom temperature and salinity are plotted at the end of the period. Linear regression yields the following best fit curves (black lines): (c) $\Delta T_b = -0.6°C - 5.8$ (°C psu^{-1}) ΔS_b ($R^2 = 0.64$) and (d) $T_b = 201.3°C - 5.0$ (°C psu^{-1}) S_b ($R^2 = 0.49$). Symbols, colors, and their size are plotted as in Figure 3. Events are plotted when $I > 2$ and coinciding temperature and salinity recordings are present, and there are (a) 47, (b) 48, (c) 44, (d) 45 events plotted.

water masses. Cooler, saltier water near the seafloor corresponds with shelf-break water which connects the onshore Lagoon Water with deeper Subtropical Lower Water (SLW) over the slope (see Figure 3 in *Andrews* [1983a] and Figure 4 in *Andrews* [1983b]). SLW has been identified with a maximum salinity of 35.7 psu at a depth of 150 m [*Andrews*, 1983a].

From the 64 intrusion events, the cooling occurs over a mean duration and standard deviation of 7.3 ± 5.4 days. The longest duration event is 25 days in April 2013 with $I = 2.6$. This event is near the threshold value for identifying intrusions and captures a period including the breakdown of the seasonal stratification followed by near-bottom cooling.

The intrusion events from PPS are compared with temperature changes from MYR at 95 and 202 m depth. The temperature decrease during an intrusion at PPS is correlated with temperature changes over the continental slope at 95 m (Figure 5a) but weakly correlated with changes at 202 m depth (Figure 5b). The duration of cooling events is correlated with the extent of temperature decreases at MYR at 95 m (Figure 5c). This relationship indicates that greater uplift in isotherms offshore leads to prolonged cooling over the outer-shelf. The correlation between the intrusion temperature at PPS and the middepth temperature at MYR indicates that the source waters come from offshore depths near 95 m (Figure 5d). From all events plotted in Figure 5d, the mean PPS intrusion temperature at 60 m, 24.1°C, is close to the mean MYR temperature at 95 m, 24.0°C. Model results will further explore source regions using temperature in section 4.2.

3.3. Along-Shelf Wind Fluctuations

Near Palm Passage, the along-shelf winds tend to be equatorward with fluctuations leading to more poleward winds during the summer monsoon (Figure 6). From ACCESS-R winds from August 2010 to July 2015,

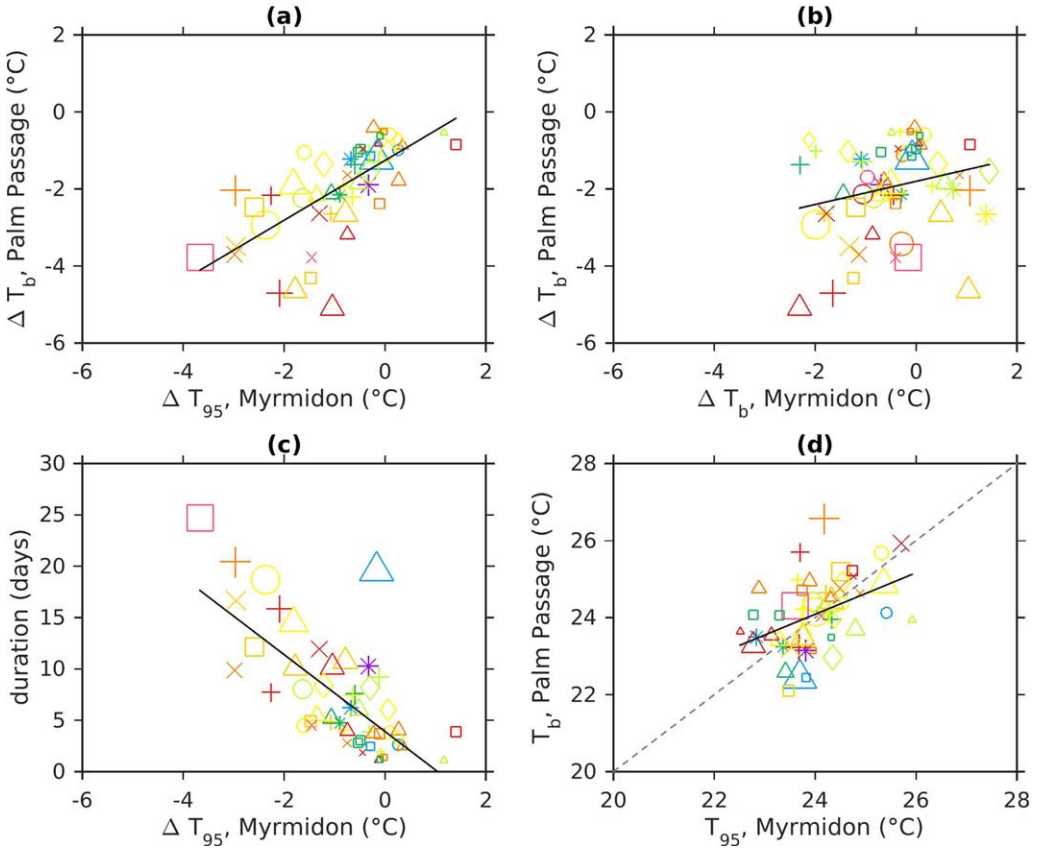

Figure 5. For each intrusion event, the temperature change at (a) ~95 m depth and (b) ~202 m from MYR is plotted against the change in near-bottom temperature from PPS. (c) The duration of the cooling period recorded from PPS is plotted again the temperature change at ~95 m from MYR. (d) The near-bottom temperature from PPS is plotted against the temperature at ~95 m from MYR at the end of the cooling period. The one-to-one (grey, dashed) curve is plotted for reference. The best fit, linear regression curves (black) are: (a) $\Delta T_{b,\ PPS} = -1.3°C + 0.8\ \Delta T_{95,\ MYR}$ ($R^2 = 0.46$) (b) $\Delta T_{b,\ PPS} = -1.8 + 0.3\ \Delta T_{b,\ MYR}$ ($R^2 = 0.06$), (c) duration = 3.9 days–3.7 days $°C^{-1}\ \Delta T_{95,\ MYR}$ ($R^2 = 0.51$), (d) $T_{b,\ PPS} = 11.2°C + 0.5\ T_{95,\ MYR}$ ($R^2 = 0.06$).

the time-mean, zonal wind stress is -0.064 N m^{-2} (-0.011 N m^{-2} cross-shelf) and the meridional wind stress is $+0.040$ N m^{-2} ($+0.075$ N m^{-2} along-shelf). During austral summer, the monthly mean along-shelf wind stress and standard deviation are $+0.037 \pm 0.071$ N m^{-2} (December), $+0.043 \pm 0.105$ N m^{-2} (January), and $+0.070 \pm 0.120$ N m^{-2} (February). The monthly mean along-shelf wind stress is a minimum in December and reaches a maximum in May ($+0.112$ N m^{-2}). From September to March, the standard deviation is greater than the monthly mean along-shelf wind stress and reaches its peak value in February. The more variable winds during austral summer include poleward bursts, impacting the velocity field and the intrusions.

The intrusion events are classified as occurring during either: (i) poleward winds, (ii) weakening equatorward winds, or (iii) strengthening equatorward winds. The event occurs in (i) if the mean along-shelf wind stress is poleward, in (ii) if the mean along-shelf wind stress is equatorward and more than half the cooling period has decreasing equatorward winds, and in (iii) if neither of the above are satisfied. The bottom intrusion index is plotted against the mean along-shelf winds (Figure 7) to indicate how the wind fluctuations control the intrusions. Of the 64 intrusion events, (i) 18 events have mean poleward winds. Of the 46 other intrusion events, (ii) 33 events have weakening equatorward winds, and (iii) 13 events have strengthening equatorward winds. Hence, most intrusion events, 80%, are either in categories (i) or (ii).

Poleward winds are important in causing near-bottom intrusions by driving poleward currents over the shelf and slope. Poleward currents can induce an onshore bottom Ekman flow that advects cooler water onshore. Over the 6 years, poleward winds occur 11% of the time and 25% of the time from December to

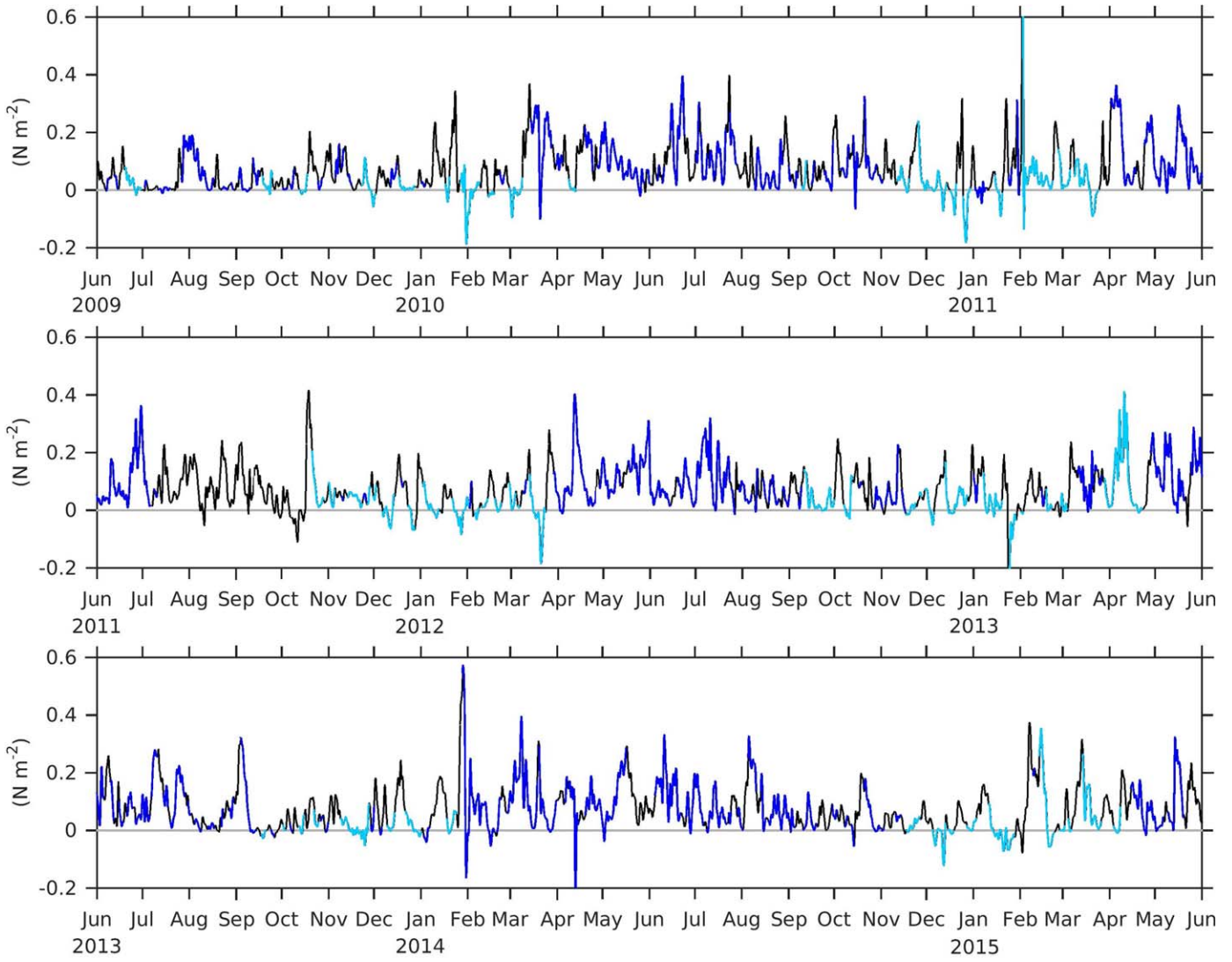

Figure 6. Low-pass filtered along-shelf winds from the Myrmidon Reef weather station (June 2009 to July 2010) and ACCESS-R (August 2010 to May 2015). Curves are black when T_b increases, blue when T_b decreases, and light blue during intrusion events. The grey line corresponds to zero along-shelf wind stress. Equatorward winds are positive and poleward winds are negative.

February. Although poleward winds are a small fraction of the total time, intrusion events occur 50% of the time when present.

Although equatorward winds are generally associated with being downwelling favorable, approximately half of the intrusion events are recorded during weakening equatorward winds. As the equatorward winds relax, an opposing along-shore pressure gradient induces poleward acceleration in the along-shore flow [*Andrews and Furnas*, 1986; *Brinkman et al*., 2002] and potentially onshore flow. Fewer intrusion events occur during periods when the mean winds are equatorward and strengthening for more than half the cooling period (iii). However, the mean magnitude of the along-shelf wind stress is small, $+0.0173$ N m^{-2}, from these 13 events. Most cases correspond with either initially weakening equatorward winds or weak equatorward winds followed by a prolonged strengthening. The initial stages of both situations are conducive to intrusions. In section 4, the model output is used to investigate the causes of intrusions from different wind categories.

3.4. Outer-Shelf Velocity Fluctuations

From PPS, the depth-averaged cross-shelf velocity, u_d, (-2 cm s^{-1}) is weaker than the along-shelf velocity, v_d, (-5 cm s^{-1}) in the annual mean (Figure 8). The best fit annual cycle is determined by applying harmonic

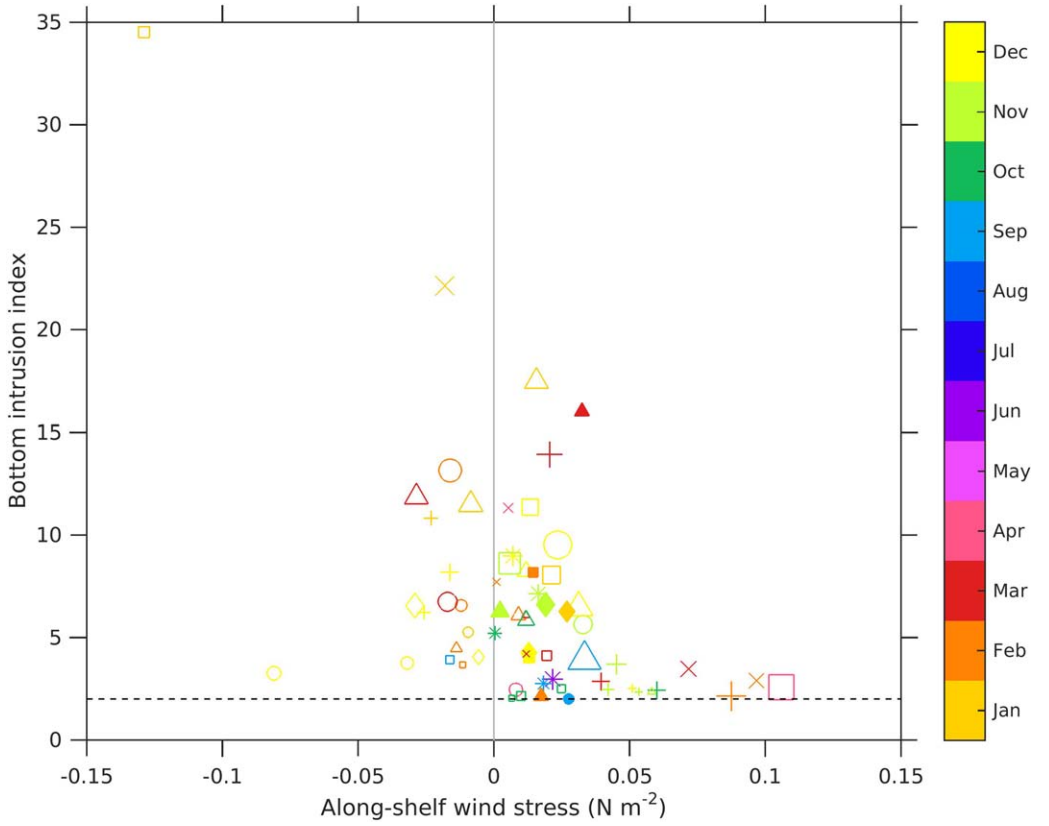

Figure 7. The bottom intrusion index plotted against the mean along-shelf wind stress for I > 2. The years plotted are 2009 (*), 2010 (o), 2011 (+), 2012 (triangle), 2013 (square), 2014 (diamond), and 2015 (×). The colors indicate the month when the intrusion occurs. The size of the symbols indicate the cooling duration, ranging from 1 day (smallest) to 25 days (largest, April 2013). The symbols are either filled or have a thicker line for intrusions in category (iii). The dashed line indicates the threshold value I = 2. The thin grey line separates poleward (negative values) and equatorward wind stress (positive values).

regression to the low-pass filtered time series. The peak poleward (equatorward) velocity occurs in October (April), which is consistent with findings from a 1985 time series in Palm Passage [*Burrage et al*., 1991]. The cross-shelf velocity u_d tends to be onshore and shows weak seasonal fluctuations, and the trend may be caused by sensitivity to choice of local coordinate system [*Brink*, 2016].

From October to March, the mean along-shelf velocity is weak (-1 cm s^{-1}). However, during the intrusion events, the mean v_d strengthens to -6 cm s^{-1} and is poleward 71% of the time. This indicates that the intrusions are linked with anomalous poleward flow over the outer-shelf. The cross-shelf velocity u_d during intrusions (-4 cm s^{-1}) is not significantly different to the mean during these months and is onshore 81% of the time.

Lagged cross-correlation is applied to the low-pass filtered velocity and wind fields. The along-shelf velocity v_d lags the along-shelf winds by 11 h, consistent with the 9–12 h time lag found for nearby near-shore and midshelf moorings in *Burrage et al*. [1991]. The correlation is statistically significant at greater than the 99% level based on the method described in *Sciremammano* [1979]. In the first 24 h of the intrusion events, the along-shelf wind stress decreases in 80% of events, with a mean change -0.02 N m^{-2} d^{-1}. There is a corresponding decrease in v_d in 70% of events, with a mean change -5 cm s^{-1} d^{-1}. When v_d is initially poleward, the velocity tends to either intensify poleward or remain poleward throughout the event (Figure 8c). When v_d is initially equatorward, almost all events show a poleward reversal (Figure 8d).

In the last 24 h, the along-shelf wind stress increases equatorward in 80% of events, with a mean change of $+0.02$ N m^{-2} d^{-1}. The along-shelf velocity v_d tends to increase equatorward (Figures 8c and 8d) as well, indicating that increasing along-shelf wind stress and velocity are related to the end of near-bottom cooling. The cross-shelf velocity u_d does not show a change correlated with winds or along-shelf velocity near

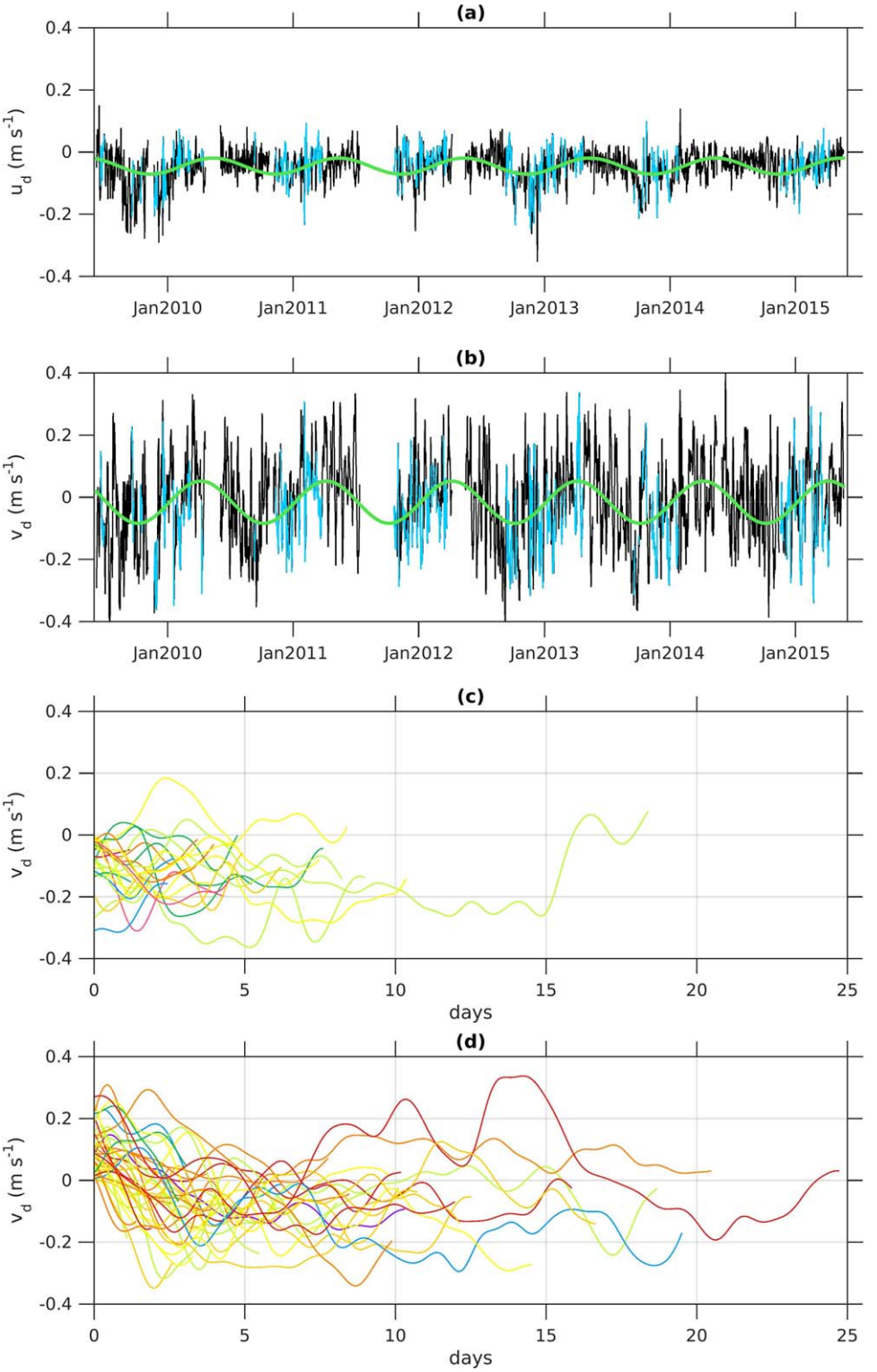

Figure 8. The (a) depth-averaged cross-shelf velocity, u_d, (m s^{-1}) and (b) depth-averaged along-shelf velocity, v_d, (m s^{-1}) at PPS. The velocity curves are light blue during the intrusion events. The best fit annual cycle (green curves) from harmonic regression yields an annual mean u_d of -0.016 m s^{-1}, an amplitude 0.026 m s^{-1} with peak onshore speeds in November and an annual mean v_d of -0.045 m s^{-1}, an amplitude of 0.068 m s^{-1} with peak poleward speeds in October. For each intrusion event, v_d time series are plotted with an initial poleward flow (c) or initial equatorward flow (d). The curves are colored by the month as in Figure 7.

Table 1. Intrusion Events Examined From Model Output Where *Skill* > 0.6[a]

Event number (Total Recorded Events)	Mean Date	I	$\lvert\Delta T_b\rvert$ (°C)	Cooling Duration (Days)	Wind Category	*Skill*	Bottom Onshore Flow Category	Onshore Extent of Intrusion, Isobath (m)
1 (12)	Nov 2010	5.6	2.2	8.0	ii	0.85	u_{accel}	45
2 (13)	Dec 2010	9.5	2.9	18.7	ii	0.89	u_{geo}	35
3 (17)	Feb 2011	2.2	2.0	20.5	ii	0.80	u_{accel}	39
4 (18)	Mar 2011	2.9	2.2	7.8	ii	0.94	u_{accel}	35
5 (19)	Mar 2011	13.9	4.7	15.8	ii	0.88	u_{accel}	34
6 (20)	Oct 2011	2.4	1.4	7.6	ii	0.75	u_{accel}	70
7 (24)	Dec 2011	2.5	0.5	1.9	iii	0.80	u_{geo}	48
8 (26)	Dec 2011	6.2	1.9	4.0	i	0.61	u_{geo}	39
9 (28)	Jan 2012	11.5	2.7	10.7	i	0.77	u_{geo}	34
10 (32)	Mar 2012	16.0	3.2	4.0	iii	0.85	u_{geo}	8
11 (34)	Mar 2012	11.9	5.1	10.2	i	0.61	u_{geo}	18
12 (39)	Dec 2012	8.2	2.2	5.5	ii	0.78	u_{geo}	34
13 (40)	Dec 2012	6.5	1.9	14.5	ii	0.63	u_{geo}	49
14 (41)	Jan 2013	8.1	2.5	12.1	ii	0.76	u_{geo}	41
15 (42)	Jan 2013	34.5	4.3	4.9	i	0.82	u_{geo}	34
16 (44)	Feb 2013	8.2	2.4	3.7	iii	0.82	u_{geo}	34
17 (46)	Apr 2013	2.6	3.8	24.7	ii	0.90	u_{geo}	3
18 (50)	Oct 2013	2.5	1.0	2.8	ii	0.93	u_{geo}	34
19 (51)	Nov 2013	8.6	2.0	18.4	ii	0.86	u_{accel}, u_{geo}[b]	34
20 (54)	Jan 2014	6.3	2.3	6.2	iii	0.61	u_{geo}	46
21 (56)	Dec 2014	6.6	1.4	8.4	i	0.91	u_{geo}	20
22 (59)	Jan 2015	22.2	3.5	16.6	i	0.63	u_{geo}	34
23 (60)	Feb 2015	2.9	3.7	9.9	ii	0.89	u_{Ekman}	18
24 (63)	Mar 2015	3.5	2.6	12.0	ii	0.95	u_{geo}	10
25 (64)	Apr 2015	11.3	3.8	4.5	ii	0.63	u_{geo}	34

[a]Wind category: (i) poleward; (ii) equatorward, relaxing; and (iii) equatorward, strengthening. Events 1, 10, 15, and 19 (in bold) are described in section 4. The bottom onshore flow category lists the main contribution to the time-mean, onshore flow over the bottom 20 m, according to (3). The intrusion's onshore extent is defined by the minimum depth of cooling, $\Delta T_b < 0$.
[b]In Event 19, u_{accel} and u_{geo} have equal contribution.

the start or end of the event. The PPS mooring may not adequately record the near-bottom cross-shelf velocity. The cross-shelf velocity can have a baroclinic contribution, including a near-bottom onshore flow, and is further examined in the model solutions.

4. Model: Intrusion Examples and Forcing Mechanisms

The eReefs model output captures the near-surface summertime warming and the timing and intensity of cooling for the bottom intrusions (Figure 2). Of the 53 events that occur during the eReefs model run time, there are 25 events that have a skill score greater than 0.6 for T_b (Table 1). Events 1, 10, 15, and 19 are discussed in detail to illustrate the processes involved during an event. Of the events recorded in Table 1, Event 1 (November 2010) has a typical cooling intensity and duration, Event 10 (March 2012) has a large bottom intrusion index I and a short duration, Event 15 (January 2013) has the greatest I, and Event 19 (November 2013) has one of the longest durations with medium I.

4.1. Along-Shelf and Onshore Spatial Extent

During Events 1, 10, 15, and 19, the sea surface temperature (SST) increased over a large portion of the Central GBR shelf and offshore with warming up to 2°C (not shown). Meanwhile, the temperature along the seafloor revealed a dramatically different evolution with tongues of cool water intruding onto the shelf (Figure 9). In the channels, near-bottom temperature decreased by up to 5°C. These intrusions extend coherently over hundreds of kilometers along-shelf, from Trinity Opening to Flinders Passage.

Between Magnetic and Flinders Passages, intrusions' onshore movement is impeded at depth by reef structures. Intrusions reach midshelf waters there by entering through Palm and Magnetic Passages into the lagoon with speeds of 10–30 cm s^{-1}. The near-bottom flow steers around the bathymetric features to the south, contributing to the spread of cool water (Figure 10). An onshore flow and southward deflection in intrusions have been recorded previously [*Andrews and Furnas*, 1986]. This near-bottom onshore flow is not reflected in the near-surface velocity, which is dominated by the poleward EAC along the slope and a mean

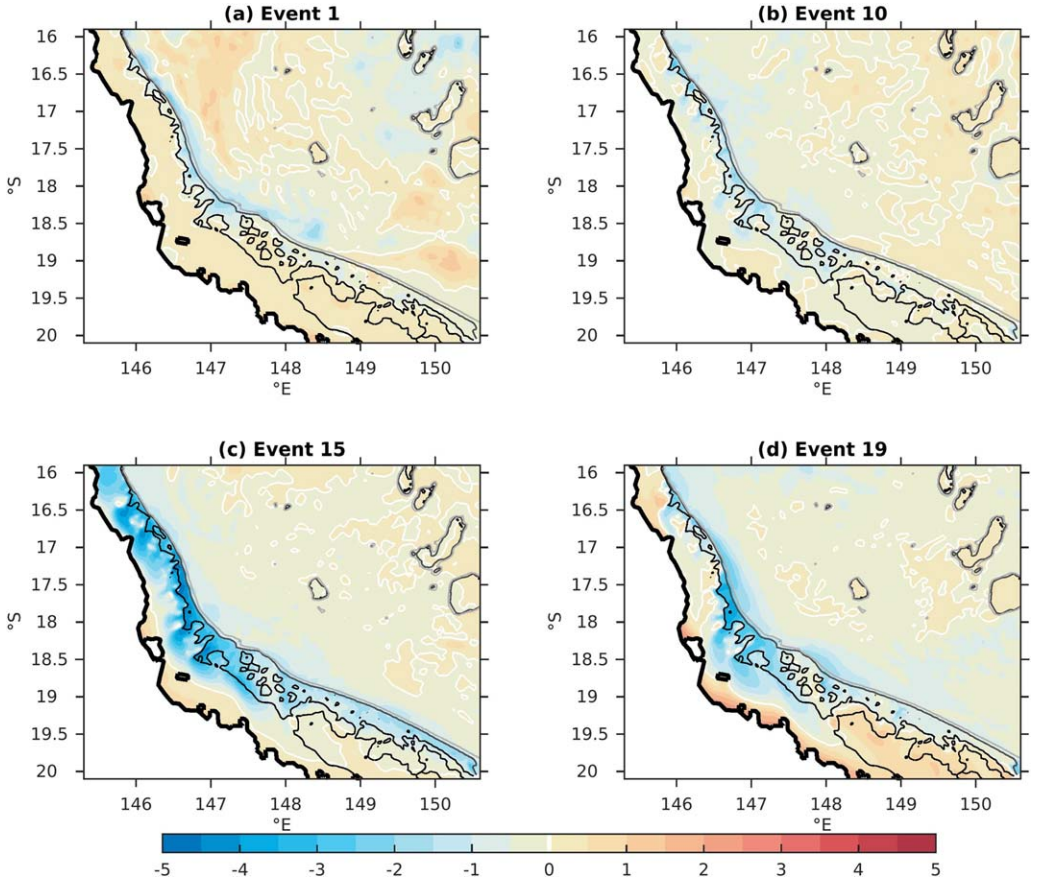

Figure 9. The change in temperature from the start to end of the intrusion is plotted from the bottom grid cell on the shelf and upper slope and at 160 m depth further offshore. The examples are (a) Event 1 (11 November to 19 November 2010), (b) Event 10 (29 February to 4 March 2012), (c) Event 15 (24 January to 29 January 2013), and (d) Event 19 (9 November 2013 to 27 November 2013). The model bathymetry contours are: 0 (thick black curve), 50 m (thin black curve), 100 m (dark grey curve), and 200 m (light grey curve).

poleward flow along the shelf (not shown). For Events 10, 15, and 19, the EAC is stronger near the surface than at 160 m depth, especially for Event 15 which reveals an equatorward current at this depth (Figure 10c).

For each event, the intrusion's onshore extent is determined along the Palm Passage cross-shelf transect (Table 1). This isobath is determined from where there is zero change in bottom temperature from the initial and final times. The intrusions extend onshore to a mean depth and standard deviation of 33 $\pm$ 14 m, corresponding to 71 $\pm$ 24 km onshore of the shelf break at 80 m depth. The onshore extent does not appear correlated with the intrusion index, cooling intensity, or event duration. Along the cross-shelf transect, most intrusions are limited to offshore of 34 m depth, just prior to Palm Island. Intrusions can extend into nearshore waters by sweeping around Palm Island from the north (Events 10, 12, 21, 23, and 24). The intrusion's onshore speed is calculated by tracking the onshore propagation of isotherms. In most cases, the onshore speed is fastest at the intrusion's leading edge and is on the order of 10 cm s^{-1}, similar to previously reported propagation speeds [*Andrews and Furnas*, 1986; *Andrews and Gentien*, 1982].

4.2. Source Waters From the East Australian Current

Preceding an intrusion event, the temperature and velocity over the shelf and slope have different configurations which may precondition the shelf for intrusive upwelling. At midshelf, waters may be well mixed initially (Events 1, 15, and 19 (Figure 11), and Events 2, 3, 13–17, 20, and 22–24). Other events have stratified waters over the shelf (Event 10 (Figure 11), and Events 6, 7, 9–12, 21, and 25). In some cases (Events 10, 15, and 19 (Figure 11), and Events 3–5, 8, 16, and 18), cross-shelf temperature gradients occur near the shelf

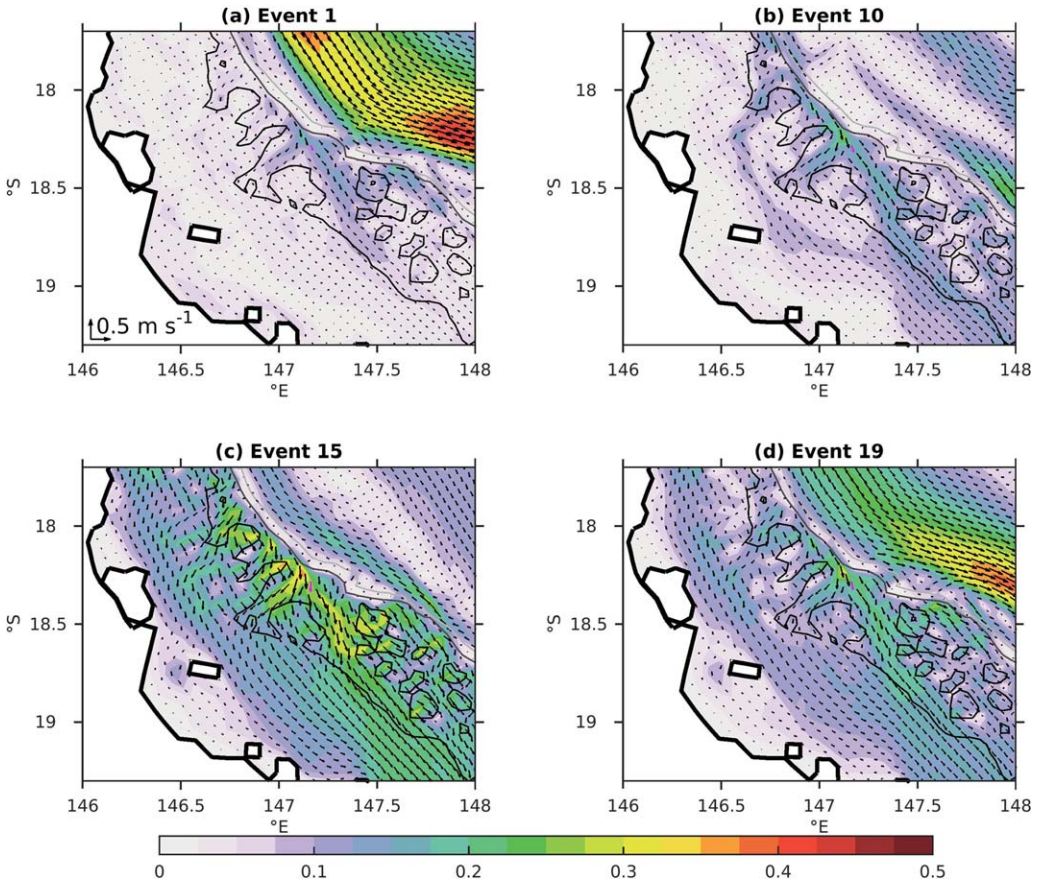

Figure 10. The velocity (arrows, speed shaded) depth-averaged over the whole water column for depths shallower than 20 m, over the bottom 20 m on the shelf and upper slope, and at 160 m further offshore. The pink arrow corresponds to the near-bottom velocity closest to the Palm Passage mooring site. The thick black curves indicate land applied in the model bathymetry.

break with warmer water onshore. In some of these cases, the cooler waters spreading onto the shelf have their origins more directly offshore rather than from greater depths below the shelf break (80 m).

The offshore source of the bottom waters is determined by tracing the change in position of bottom temperature from the shelf break at the peak of the intrusion to offshore of the shelf break at the start of the intrusion. This measures the greatest depth of offshore waters that flow onto the continental shelf. Intrusions originate from a mean depth and standard deviation of 107 $\pm$ 13 m, corresponding to isotherm uplift of 27 $\pm$ 13 m from below the shelf break. For Events 1, 10, 15, and 19, uplift to the shelf break is 32, 21, 40, and 66 m, respectively (Figure 11), and 66 m is the largest uplift from all events. The greatest bottom cooling tends to occur at the shelf break. Cooling decays with depth, and uplift is confined closer to the shelf break. By 200 m depth along the slope, some cases (Events 3, 6–8, 13, 15, and 19) reveal increases in bottom temperature. These solutions support the observations that the bottom temperature at 200 m depth does not necessarily reflect the uplift associated with intrusions.

During most of the events, the EAC core speed increases poleward near the surface and its core tends to shift toward the slope (e.g., Events 1, 10, and 19 in Figure 11). This change is consistent with the uplift in isotherms over the slope. The isotherm tilt corresponds to geostrophic vertical shear causing the flow to intensify poleward near the surface. Near the 200 m isobath, the EAC speeds are inshore of the jet core but this location is able to capture fluctuations in the EAC jet speed. Below 200–300 m, an equatorward undercurrent is present during some events with speeds reaching 0.4 m s^{-1}. Almost all cases indicate that the depth-averaged, along-shelf velocity near 200 m intensifies poleward during the intrusion event, with a mean speed increase of 0.12 m s^{-1}. The exceptions are Events 1 (Figures 11a and 11b), 3, and 7, in which equatorward flow emerges at depth. Although both uplift and intensifying EAC speeds tend to occur during

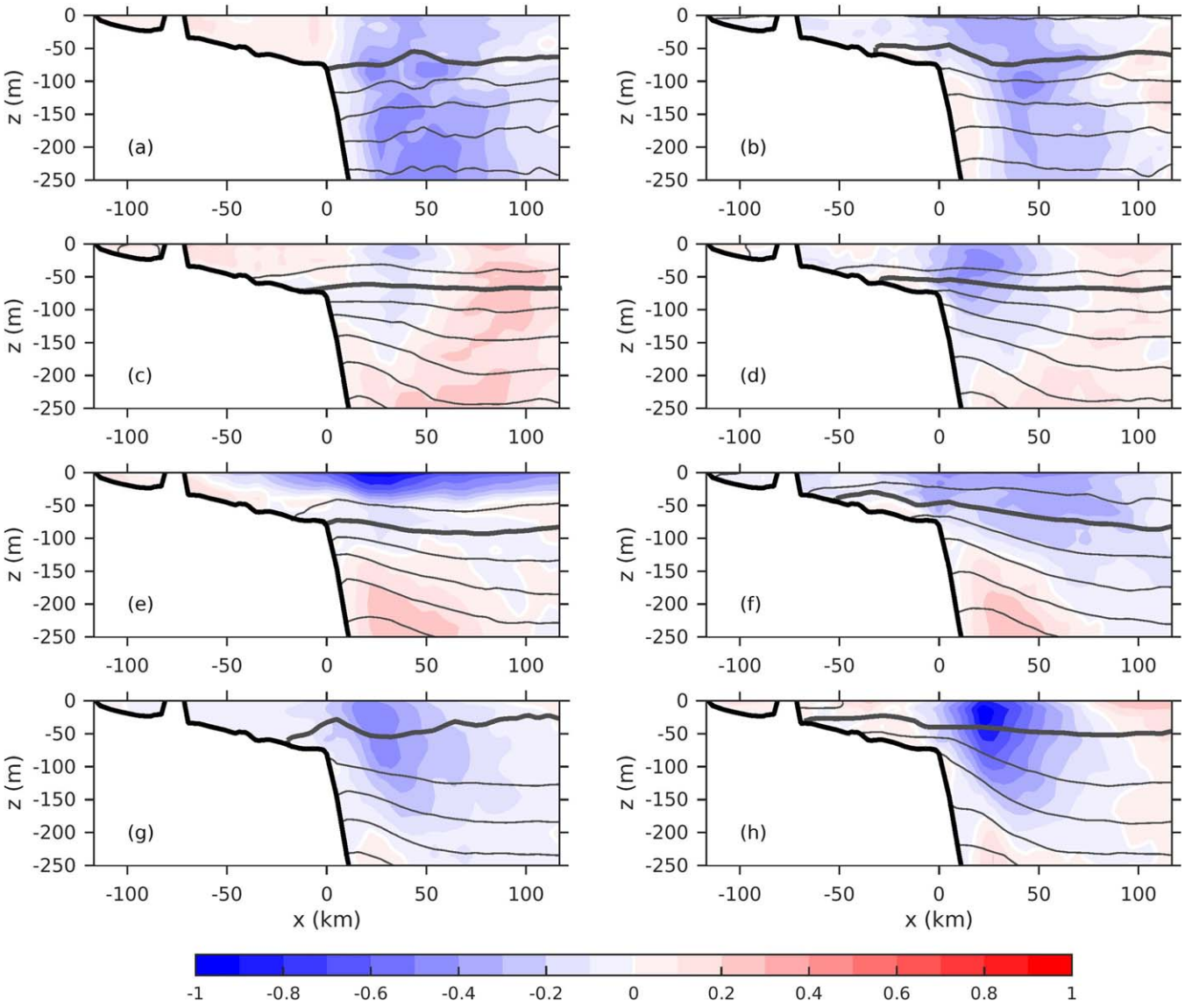

Figure 11. Cross sections of along-shelf velocity (shaded) (m s^{-1}) and temperature (grey curves) are shown at the start (left column) and end (right column) of the cooling period. The examples correspond to Events (a, b) 1, (c, d) 10, (e, f) 15, and (g, h) 19. Isotherms are plotted every 2°C (thin grey curve), and the 26°C isotherm (thick grey curve) and model bathymetry (thick black curve) are included. The cross-shelf distance is with respect to the shelf break at 80 m (147.1173°E, 18.2126°S) oriented along the cross-shelf transect in Figure 1.

intrusion events, results do not indicate a clear correlation between them. The solutions support that as the EAC intensifies poleward, uplift leads to the transport of cool water onto the shelf from depth.

4.3. Outer-Shelf Temperature and Salinity Fluctuations

Time series of along-shelf wind stress, temperature, salinity, and velocity are plotted from the outer-shelf location (72 m) at the closest grid point (~3 km distance) to the Palm Passage mooring site (Figure 12). In the examples, along-shelf wind stress is categorized as (i) poleward in Event 15, (ii) equatorward and weakening in Events 1 and 19, and (iii) equatorward and strengthening in Event 10. The cooling durations are either typical (Event 1), short (Events 10 and 15), or long (Event 19) compared with other events.

These examples show intrusions (Figures 12e–12h) occurring over the bottom 10–30 m. Their mean height and standard deviation is 23 $\pm$ 13 m from both temperature and salinity. Bottom salinity increases in Events 10, 15, and 19 (Figures 12j–12l). While a small salinity decrease occurs in Event 1 (Figure 12i), bottom salinity increases further onshore and observations indicate an increase. Similar to the observations (Figure 4c),

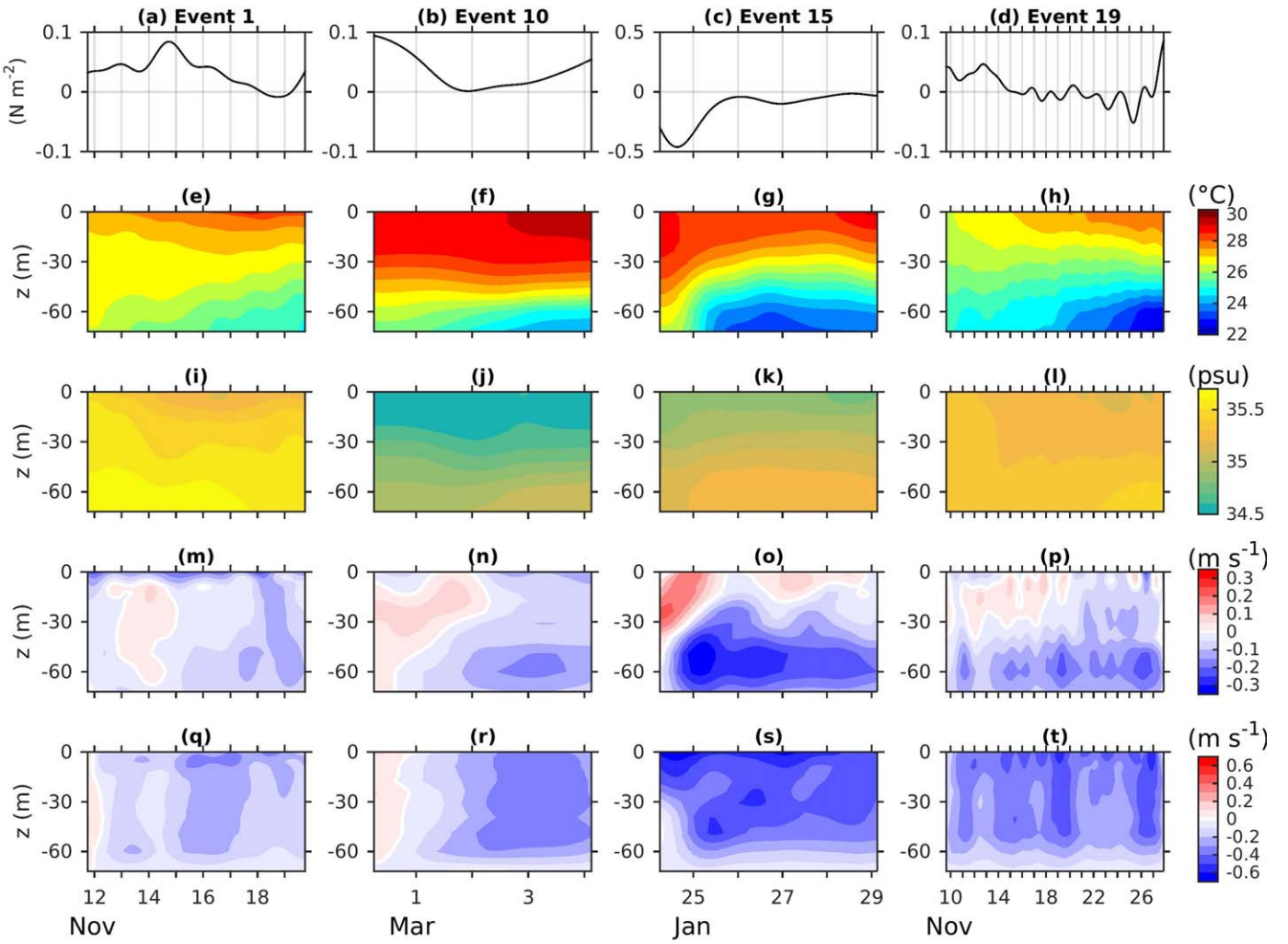

Figure 12. Time series are plotted for Events (a, e, i, m, q) 1, (b, f, j, n, r) 10, (c, g, k, o, s) 15, and (d, h, l, p, t) 19 at the outer-shelf of the Palm Passage transect (72 m). The fields are plotted for the event duration and correspond to (a–d) along-shelf wind stress, (e–h) temperature, (i–l) salinity, (m–p) cross-shelf velocity, and (q–t) along-shelf velocity.

bottom salinity increases during most events. From all available salinity data during intrusions in Table 1, the total Skill is 0.82 (0.80) for near-surface (near-bottom) salinity.

During almost all intrusion events considered in the model, the SST tends to increase as the bottom temperature decreases as illustrated over the outer-shelf in Figures 12e, 12f, and 12h. The only exception is Event 15 (Figure 12g) during a large poleward wind burst, which will be discussed in section 5. In observations and the model, the intensity of surface temperature warming is not correlated with the intensity of bottom temperature cooling despite both occurring simultaneously. Surface warming is weakly correlated with wind stress, with increasing surface temperatures for decreasing mean along-shelf wind stress.

4.4. Along-Shelf Momentum Balance

While observations at PPS indicate that along-shelf wind fluctuations control the along-shelf velocity during intrusions, they do not provide a complete picture of the cross-shelf circulation. The model results can be used to further understand the causes for near-bottom onshore flow during intrusions. When the along-shelf wind stress is equatorward, a surface Ekman current is directed onshore as in Events 1, 10, and 15 (Figure 12). Although these winds are downwelling favorable, the along-shelf velocity is poleward and an onshore flow emerges near the bottom. In all events, the near-bottom current is onshore when the along-shelf current is equatorward (e.g., Figures 12m–12t). Compared with depth-averaged currents at PPS, the model's cross-shelf velocity mean bias, 0.001 m s^{-1}, is small and the model's along-shelf velocity mean bias,

$-0.10\ \mathrm{m}^{-1}$, favors stronger poleward flow during intrusions. From all intrusions in Table 1, the total Skill is 0.52 (0.70) for depth-averaged cross-shelf (along-shelf) velocity. Similar with observations, the model's poleward velocity tends to weaken near the end of the cooling event as the along-shelf winds tend to increase equatorward (Figure 12). While winds play an important role in modulating the along-shelf current over the outer-shelf, they do not fully explain the cross-shelf circulation. The dynamics of the near-bottom cross-shelf flow is important for controlling how intrusions propagate onto the shelf.

To determine the mechanisms controlling the cross-shelf circulation, the along-shelf momentum balance is used to decompose the cross-shelf flow into geostrophic and ageostrophic contributions:

$$u = \underbrace{-\frac{1}{f}\frac{dv}{dt}}_{u_{accel}} + \underbrace{\left\{-\frac{1}{f}\ \boldsymbol{u}\cdot\nabla v\right\}}_{u_{adv}} + \underbrace{\left\{-\frac{1}{f\rho}\frac{\partial p}{\partial y}\right\}}_{u_{geo}} + \underbrace{\frac{1}{f}\nabla_H\cdot(\nabla_H \nu_H\ v)}_{u_{hdiff}} + \underbrace{\frac{1}{f}\frac{\partial}{\partial z}\left(\nu_v\frac{\partial v}{\partial z}\right)}_{u_{Ekman}}, \tag{3}$$

where f is the Coriolis parameter, ∇_H is the horizontal gradient operator, ν_H is the horizontal eddy viscosity, and ν_V is the vertical eddy viscosity. The along-shelf and cross-shelf velocity have vertical variations over the bottom 20 m, reducing in speed near the seafloor. Hence, the velocity contributions are output from the model diagnostics, depth-averaged over the bottom 20 m, and time-averaged over each event. The bottom velocity from horizontal diffusion, u_{hdiff}, is a negligible contribution to the near-bottom onshore flow (Figures 13m–13p). The bottom velocity from momentum advection, u_{adv}, is directed offshore and greatest at the edge of the bottom Ekman layer (Figures 13e–13h). For each event, the bottom onshore flow is mainly due to ageostrophic, u_{accel} and u_{Ekman}, and geostrophic, u_{geo}, contributions. The leading contribution is labeled in Table 1.

There are several processes that induce onshore flow. First, an onshore ageostrophic flow, $u_{accel} < 0$, occurs when the along-shelf flow accelerates poleward due to weakening equatorward winds or poleward winds. This process tends to have a dominant contribution at some point during most intrusions, usually early on in the cooling period, and throughout the water column. In Figures 13a–13d, u_{accel} is a dominant contribution to bottom onshore flow in Events 1 and 19. Second, the bottom Ekman flow is onshore, $u_{Ekman} < 0$, when the geostrophic along-shelf flow is poleward near the bottom. While previous studies have suggested that intrusions occur by a bottom Ekman flow [e.g., *Andrews and Gentien*, 1982; *Andrews and Furnas*, 1986], u_{Ekman} is the dominant contribution to bottom onshore flow in only Event 23. In Figures 13q–13t, u_{Ekman} has greatest onshore speeds when the poleward current has its greatest speeds (Figures 12q–12t) but plays a secondary contribution to the total onshore bottom flow.

Instead, the diagnostics indicate that a third process plays a significant role in most intrusion events (Table 1). When more buoyant water is present equatorward, an along-shelf density gradient causes vertical shear in the geostrophic cross-shelf flow with a tendency for onshore flow at depth, $u_{geo} < 0$. In most cases, this bottom-intensified onshore flow occurs during the cooling period when the intrusion has encroached onto the shelf and occurs over the intrusion's vertical scale (Figures 13i–13l). An along-shelf section indicates that the bottom-intensified flow is greatest through Palm and Magnetic Passages and present in the channels to the north (Figures 14a–14d). The vertical circulation shows intense downward flow to the north of the passages and upward flow to the south (Figures 14i–14l). This vertical flow causes an isopycnal tilt, with dense water lifted upward to the south (Figures 14m–14t). Both salty and cool water can contribute to this isopycnal tilt, in addition to pre-existing background along-shelf temperature and salinity gradients. This feedback between the density field and the circulation provides a mechanism to enhance the onshore spread of the intrusion through the reef passages.

5. Discussion

Observations and model analyses support that winds modulate intrusive upwelling on synoptic, seasonal, and interannual timescales. Over the 6 years, the event that had the greatest bottom intrusion index (Event 15 in Table 1) occurred during Cyclone Oswald. In late January 2013, the southward passage of Cyclone Oswald led to strong poleward winds over the Central GBR (Figure 12c) and heavy rainfall and flooding [*Bureau of Meteorology*, 2013]. This extreme wind led to bottom cooling all along the Central GBR shelf-edge (Figure 9c), especially in the near-shore regions adjacent to and north of Palm Passage.

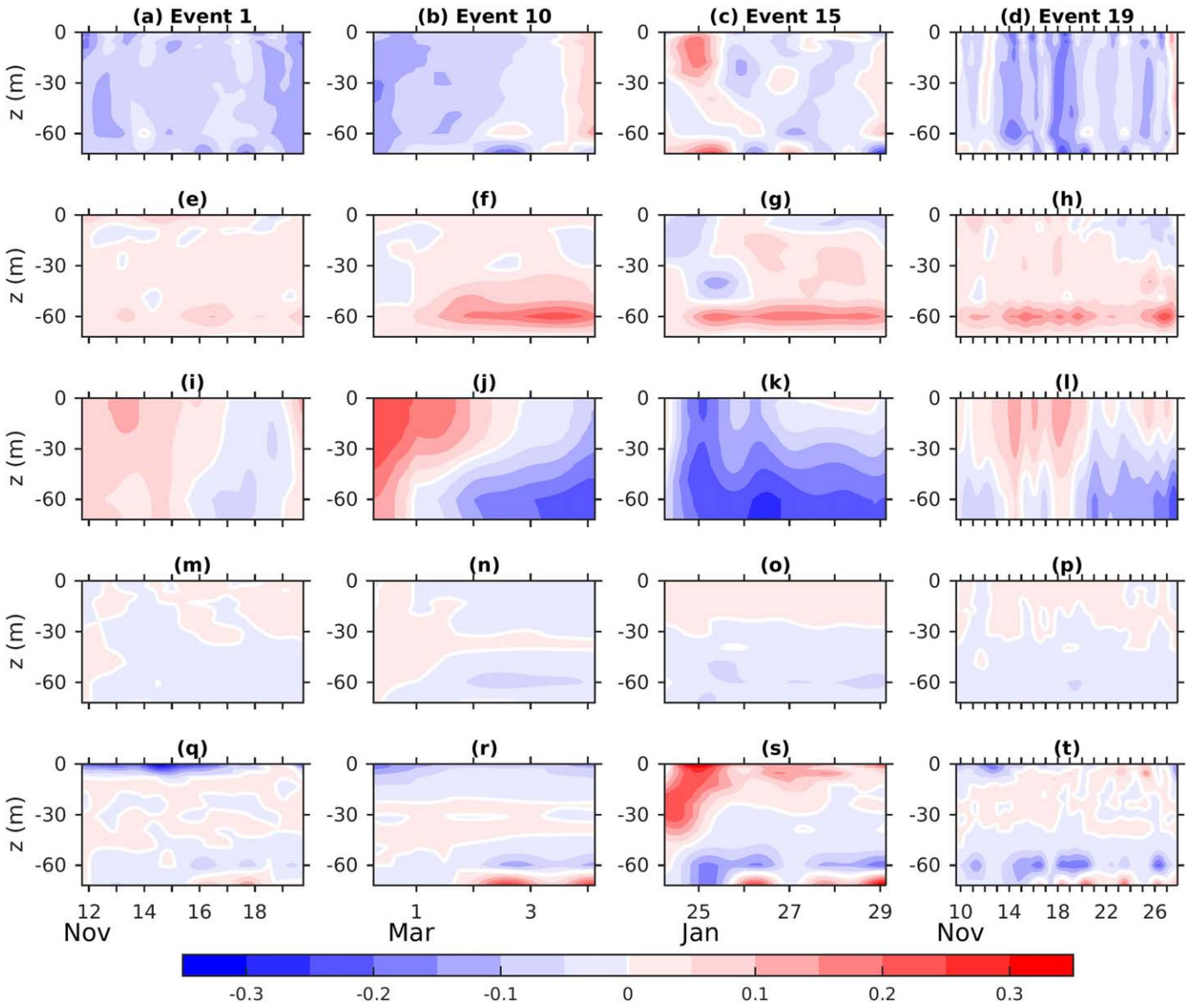

Figure 13. From the model diagnostics, the contributions to the cross-shelf velocity (m s^{-1}) from Figures 12m–12p are plotted for Events 1, 10, 15, and 19. The contributions are from the following terms in equation (3): (a–d) u_{accel}, (e–h) u_{adv}, (i–l) u_{geo}, (m–p) u_{hdiff}, and (q–t) u_{Ekman}.

Seasonally, intrusions occur primarily from October to March, when the southeasterly trade winds are displaced southward and winds in the Central GBR are more variable due to northwesterly monsoon winds [*Redondo-Rodriguez et al*., 2012]. In Palm Passage, the along-shelf velocity responds within a day to along-shelf wind fluctuations, accelerating poleward during intrusion events. Intrusive upwelling through Palm Passage and adjacent channels between reefs display similar dynamical characteristics to upwelling through submarine canyons. Correspondingly, isotherms uplift when the along-shelf flow is in the opposite direction of topographic wave propagation (poleward) over the mouth of the opening [*Klinck*, 1996; *Allen and Durrieu de Madron*, 2009; *Connolly and Hickey*, 2014]. As in those studies, the along-shelf flow is deflected onshore during an upwelling event. Within canyons there is an upward vertical flow and a cool anomaly on the downstream (southern) side, also found in the model results (Figures 14i–14l). While *Klinck* [1996] does not find that the surface temperature changes during upwelling, surface warming occurs in many of the intrusion events recorded here and will be discussed later on. These modeling and observational studies may inform our understanding of the drivers and temporal and spatial characteristics of intrusive upwelling through reef passages.

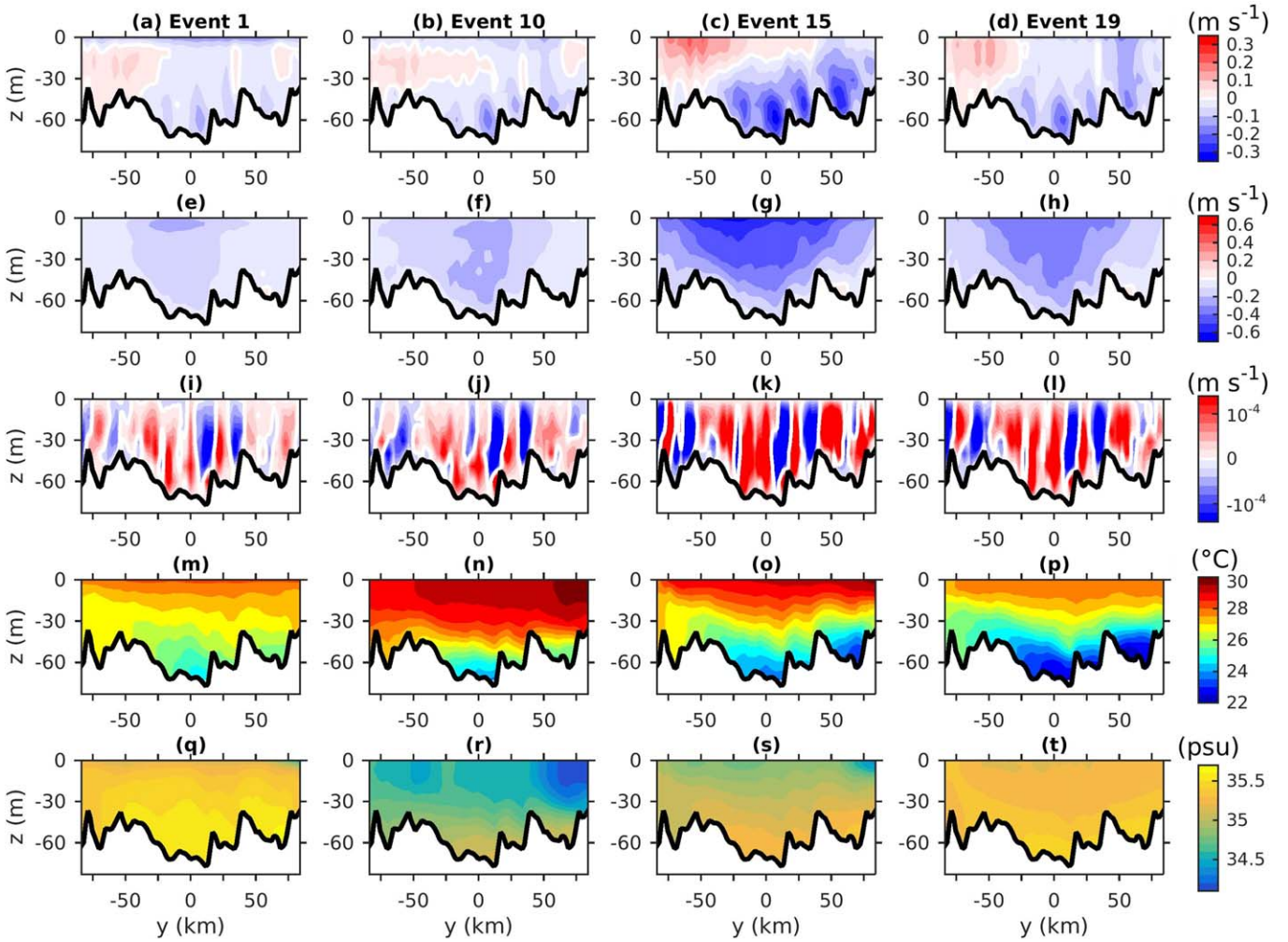

Figure 14. Along-shelf sections are plotted from Events 1, 10, 15, and 19 for the following: (a–d) time-mean cross-shelf velocity, (e–h) time-mean along-shelf velocity, (i–l) time-mean vertical velocity, (m–p) end time temperature, and (q–t) end time salinity. The model bathymetry (thick black curve) is plotted. The along-shelf distance is with respect to the closest PPS location in the model (147.1617°E, 18.2832°S) oriented along the along-shelf transect in Figure 1.

On interannual timescales, there is some evidence that the El Niño Southern Oscillation (ENSO) affects intrusive upwelling in the Central GBR. In the 1982–1983 Palm Passage study, large intrusions were detected (six events), but it was noted that the typical monsoon winds failed to develop due to El Niño and resulted in less frequent and shorter duration northerly winds [*Andrews and Furnas*, 1986]. Along the GBR, summer monsoon winds are suppressed (intensified) during El Niño (La Niña) phases [*Evans and Allan*, 1992; *Lough*, 1994; *Redondo-Rodriguez et al*., 2012]. For October through March, the mean Southern Oscillation Index (SOI) is −27.4 (negative/positive for El Niño/La Niña) for 1982–1983. In that study, there were ∼54 days during which the near-bottom temperature decreased. This total is comparable to recent El Niño years. The mean SOI is negative during 2009–2010 (−10.5; 50 upwelling days) and 2014–2015 (−7.0; 69 days). Overall there are more upwelling days recorded with positive SOI, including 2010–2011 (20.9; 84 days), 2011–2012 (9.8; 82 days), 2012–2013 (1.0; 58 days), and 2013–2014 (0.9; 47 days). Longer time records are needed to support these findings further, but these results suggest that ENSO may modulate upwelling events through changes in the wind field rather than changes in the thermocline depth.

While the intrusions spread onshore along the seafloor, they have potential feedbacks on the surface temperature. Over the shelf, the stratification increases due to cool, salty bottom water and is enhanced by weaker surface mixing during doldrum conditions. Consequently, light penetration is trapped in a thinner layer and leads to near-surface warming [*Steinberg*, 2007; *Schiller et al*., 2009; *Berkelmans et al*., 2010]. In the wet season, precipitation causes surface freshening, increasing the stratification and reducing turbulent

mixing near the surface [*Orr*, 1933]. The model results demonstrate that cool, salty intrusions increase the stratification with contributions from surface freshening (Figures 12q–12t). Consistent with these studies' hypotheses, most events reveal simultaneous surface warming, and this feedback may impact surface warming patterns in the Central GBR given the extensive along-shelf area impacted by intrusions.

6. Conclusions

From June 2009 to 2015, intrusive upwelling is detected in the Palm Passage mooring observations with 64 intrusion events identified. A bottom intrusion index is defined based on the thermal stratification and decrease in near-bottom temperature, in order to identify intrusion events in the temperature time series and to distinguish intrusion events from seasonal cooling of the water column. During events, near-bottom temperatures typically decrease by 1–3°C over 1 week and are associated with increasing near-bottom salinity originating from offshore SLW. Intrusions occur mostly from October to March, when the southeasterly trade winds relax and monsoon winds are active. Most events occur when equatorward winds weaken or winds are poleward, consistent with past studies conducted over shorter time periods [e.g., *Andrews and Furnas*, 1986]. During these periods, the along-shelf velocity tends to accelerate poleward over the outer-shelf. The velocity fluctuations indicate that this along-shelf velocity is predominantly wind-driven and controls the onset and end of bottom cooling.

The temperature and velocity observations are compared with the hydrodynamic eReefs model results for the Central GBR. Intrusion events with high skill are examined in detail and illustrate that cooling along the seafloor occurs over hundreds of kilometers. Palm Passage is a focal point for intrusive upwelling, with bottom cooling enhanced at gaps between reefs. This water flows onshore and southward, allowing it to enter onto the GBR shelf where otherwise blocked by reef structures along the shelf-edge. During events, uplift in isotherms is ∼30 m over the slope, stratifying shelf waters that may be well-mixed initially. Concurrently, the EAC intensifies poleward with its jet core shifted toward the shelf break in most cases. Fluctuations in the EAC may play a role in setting the source waters for intrusions over the shelf, since the shelf's bottom temperature and salinity originates at ∼110 m depth. The model diagnostics are used to test whether the onshore flow is Ekman-driven, as suggested in past studies [e.g., *Andrews and Gentien*, 1982]. During most events, a near-bottom onshore flow arises within Palm Passage and model diagnostics indicate that this flow is primarily geostrophic. A vertical circulation develops within the channel, with upward flow to the south causing an along-shelf isopycnal tilt. A background along-shelf density gradient may contribute to this tilt with fresher, warmer water to the north. This along-shelf isopycnal tilt balances vertical shear in the geostrophic flow with onshore flow at depth. The feedback facilitates the onshore propagation of the intrusion through the reef passages and highlights that temperature and salinity gradients contribute to this mechanism.

Future studies are needed to address the relative importance of EAC versus wind fluctuations to intrusive upwelling in the Central GBR and to compare the impact of the reef passages on shelfbreak upwelling with intrusions arising in other shelf-edge systems [e.g., *Benthuysen*, 2010; *Castelao*, 2011]. This work indicates that temperature and salinity gradients, either pre-existing or arising from the intrusion, may play an important role in the intrusion's onshore propagation and process experiments are needed to elucidate this mechanism. This study highlights the importance of continuous long-term temperature measurements to link temperature variability with climate dynamics on interannual and longer timescales. A suite of climate models project changes in Pacific western boundary currents over the coming decade, which include a weakening of the northern EAC transport [*Hu et al*., 2015]. Projections for the EAC transport and regional winds can be used to determine future changes in intrusive upwelling along the GBR. High resolution shelf downscaling of future climate scenarios provide one potential tool for assessing these changes in boundary currents and cross-shelf exchange [e.g., *Caputi et al*., 2015]. In addition, further understanding is needed of how intrusive upwelling impacts the GBR's coral reef carbonate chemistry, which is controlled by physical and biological processes on a range of timescales [e.g., *Albright et al*., 2013; *Albright et al*., 2015], given that upwelling has been linked with ocean acidification off the western North America continental shelf [*Feely et al*., 2008]. Studies are underway to understand how intrusive upwelling contributes to nutrient fluxes to the GBR lagoon and the implications for marine ecosystems.

Acknowledgments

Data were sourced from the Integrated Marine Observing System (IMOS)—IMOS is a national collaborative research infrastructure, supported by Australian Government. This data are made available through the Australian Ocean Data Network Portal (https://portal.aodn.org.au/) and the Australian Institute of Marine Science Data Catalogue (http://www.aims.gov.au/docs/data/data.html) and includes the Palm Passage mooring, Myrmidon Reef mooring, and Myrmidon Reef weather station data. The eReefs project is a collaboration between the Great Barrier Reef Foundation, Bureau of Meteorology, Commonwealth Scientific and Industrial Research Organization, Australian Institute of Marine Science and the Queensland Government, supported by funding from the Australian and Queensland Governments, the BHP Billiton Mitsubishi Alliance and the Science and Industry Endowment Fund. The eReefs model data are available through the National Computational Infrastructure public THREDDS server (http://dap.nci.org.au/). The ACCESS data and the Southern Oscillation Index (SOI) are available through the Bureau of Meteorology (http://www.bom.gov.au/). This research was supported by the Australian Institute of Marine Science. We thank the oceanographic technicians, crew of the R/V Cape Ferguson, Felicity McAllister, Paul Rigby, and Simon Spagnol for assistance with the Queensland-IMOS data and Farhan Rizwi for help with the eReefs model data. We thank Miles Furnas and two anonymous reviewers for comments on the manuscript.

References

Albright, R., C. Langdon, and K. R. N. Anthony (2013), Dynamics of seawater carbonate chemistry, production, and calcification of a coral reef flat, central Great Barrier Reef, *Biogeosciences*, *10*(10), 6747–6758.

Albright, R., J. Benthuysen, N. Cantin, K. Caldeira, and K. Anthony (2015), Coral reef metabolism and carbon chemistry dynamics of a coral reef flat, *Geophys. Res. Lett.*, *42*, 3980–3988, doi:10.1002/2015GL063488.

Allen, S. E., and X. Durrieu de Madron (2009), A review of the role of submarine canyons in deep-ocean exchange with the shelf, *Ocean Sci.*, *5*(4), 607–620.

Andrews, J. C. (1983a), Water masses, nutrient levels and seasonal drift on the Outer Central Queensland Shelf (Great Barrier Reef), *Aust. J. Mar. Freshwater Res.*, *34*, 821–834.

Andrews, J. C. (1983b), Thermal waves on the Queensland shelf, *Aust. J. Mar. Freshwater Res.*, *34*, 81–96.

Andrews, J. C., and P. Gentien (1982), Upwelling as a source of nutrients for the Great Barrier Reef Ecosystems: A solution to Darwin's question?, *Mar. Ecol. Prog. Ser.*, *8*(3), 257–269.

Andrews, J. C., and M. J. Furnas (1986), Subsurface intrusions of Coral Sea water into the central Great Barrier Reef-I. Structures and shelf-scale dynamics, *Cont. Shelf Res.*, *6*(4), 491–514.

Beaman, R. J. (2010), Project 3DGBR: A high-resolution depth model for the Great Barrier Reef and Coral Sea, *Marine and Tropical Sciences Research Facility (MTSRF) Project 2.5i.1a Final Report*, pp. 13 plus Appendix 1, MTSRF, Cairns, Australia.

Benthuysen, J. (2010), Linear and nonlinear stratified spindown over sloping topography, PhD thesis, 205 pp., Massachusetts Inst. of Technol. and Woods Hole Oceanogr. Inst., Cambridge, Mass.

Berkelmans, R., S. J. Weeks, and C. R. Steinberg (2010), Upwelling linked to warm summers and bleaching on the Great Barrier Reef, *Limnol. Oceanogr. Methods*, *55*(6), 2634–2644.

Bongaerts, P., T. Ridgway, E. M. Sampayo, and O. Hoegh-Guldberg (2010), Assessing the 'deep reef refugia' hypothesis: Focus on Caribbean reefs, *Coral Reefs*, *29*, 309–327.

Brink, K. H. (2016), Cross-shelf exchange, *Annu. Rev. Mar. Sci.*, *8*, 59–78, doi:10.1146/annurev-marine-010814-015717.

Brinkman, R., E. Wolanski, E. Deleersnijder, F. McAllister, and W. Skirving (2002), Oceanic inflow from the Coral Sea into the Great Barrier Reef, *Estuarine Coastal Shelf Sci.*, *54*(4), 655–668.

Bureau of Meteorology (2010), Operational implementation of the ACCESS Numerical Weather Prediction systems, *NMOC Oper. Bull.*, *83*, Melbourne. [Available at http://www.bom.gov.au/australia/charts/bulletins/apob83.pdf.]

Bureau of Meteorology (2013), Special Climate Statement 44—Extreme rainfall and flooding in coastal Queensland and New South Wales. [Available at http://www.bom.gov.au/climate/current/statements/scs44.pdf.]

Burrage, D. M., J. A. Church, and C. R. Steinberg (1991), Linear systems analysis of momentum on the continental shelf and slope of the central Great Barrier Reef, *J. Geophys. Res.*, *96*(C12), 22,169–22,190.

Caputi, N., et al. (2015), Management implications of climate change effect on fisheries in Western Australia, Part 1: Environmental change and risk assessment, *FRDC Proj. 2010/535, Fisheries Res. Rep.*, 260, 180 pp., Dep. of Fish., Western Australia.

Cartwright, D. E., and R. D. Ray (1990), Oceanic tides from Geosat altimetry, *J. Geophys. Res.*, *95*(C3), 3069–3090.

Castelao, R. (2011), Intrusions of Gulf Stream waters onto the South Atlantic Bight shelf, *J. Geophys. Res.*, *116*, C10011, doi:10.1029/2011JC007178.

Connolly, T. P., and B. M. Hickey (2014), Regional impact of submarine canyons during seasonal upwelling, *J. Geophys. Res. Oceans*, *119*, 953–975, doi:10.1002/2013JC009452.

Eanes, R., and S. Bettadpur (1995), The CSR 3.0 global ocean tide model, *Tech. Mem., CST-TM-95-06*, Cent. for Space Res., University of Texas, Austin, Tex.

Evans, J. L., and R. J. Allan (1992), El Niño/Southern Oscillation modification to the structure of the monsoon and tropical cyclone activity in the Australasian region, *Int. J. Climatol.*, *12*(6), 611–623.

Feely, R. A., C. L. Sabine, J. M. Hernandez-Ayon, D. Ianson, and B. Hales (2008), Evidence for upwelling of corrosive ''acidified'' water onto the continental shelf, *Science*, *320*, 1490–1492.

Furnas, M. J., and A. W. Mitchell (1996), Nutrient inputs into the central Great Barrier Reef (Australia) from subsurface intrusions of Coral Sea waters: A two-dimensional displacement model, *Cont. Shelf Res.*, *16*(9), 1127–1148.

Garrett, C. (1979), Topographic Rossby waves off east Australia: Identification and role in shelf circulation. *J. Phys. Oceanogr.*, *9*(2), 244–253.

Gill, A. (1982), *Atmosphere-Ocean Dynamics*, 662 pp., Academic, Orlando, Fla.

Glynn, P. W. (1996), Coral reef bleaching: Facts, hypotheses and implications, *Global Change Biol.*, *1*, 177–509.

Herzfeld, M. (2006), An alternative coordinate system for solving finite difference ocean models, *Ocean Modell.*, *14*(3–4), 174–196.

Herzfeld, M., and J. R. Andrewartha (2012), A simple, stable and accurate Dirichlet open boundary condition for ocean model downscaling, *Ocean Modell.*, *43–44*, 1–21.

Herzfeld, M., J. Waring, J. Parslow, N. Margvelashvili, P. Sakov, and J. Andrewartha (2008), SHOC: Sparse Hydrodynamic Ocean Code Science manual, *CSIRO internal document*, 121 pp.

Herzfeld, M., et al. (2013), *eReefs WP3 Marine Modelling: Phase I Report*, 273 pp., CSIRO, Hobart.

Herzfeld, M., et al. (2014), *eReefs WP3 Marine Modelling: Phase II Interim Report*, 356 pp., CSIRO, Hobart.

Hobday, A. J., et al. (2016), A hierarchical approach to defining marine heatwaves, *Prog. Oceanogr.*, *141*, 227–238.

Hu, D., et al. (2015), Pacific western boundary currents and their roles in climate, *Nature*, *522*(7556), 299–308.

Klinck, J. M. (1996), Circulation near submarine canyons: A modeling study, *J. Geophys. Res.*, *101*(C1), 1211–1223.

Kundu, P. K., and J. S. Allen (1976), Some three-dimensional characteristics of low-frequency current fluctuations near the Oregon coast, *J. Phys. Oceanogr.*, *6*(2), 181–199.

Lough, J. M. (1994), Climate variation and El Niño-Southern Oscillation events on the Great Barrier Reef: 1958 to 1987, *Coral Reefs*, *13*(3), 181–185.

Oke, P. R., G. B. Brassington, D. A. Griffin, and A. Schiller (2008), The Bluelink ocean data assimilation system (BODAS), *Ocean Modell.*, *21*(1), 46–70.

Orr, A. P. (1933), Physical and chemical conditions in the sea in the neighbourhood of the Great Barrier Reef, *Sci. Rep. of the Great Barrier Reef Expedition 1928–1929*, 2(3), pp. 37–86, Br. Museum of Natl. Hist., London, U. K.

Redondo-Rodriguez, A., S. J. Weeks, R. Berkelmans, O. Hoegh-Guldberg, and J. M. Lough (2012), Climate variability of the Great Barrier Reef in relation to the tropical Pacific and El Niño-Southern Oscillation, *Mar. Freshwater Res.*, *63*, 34–47.

Riegl, B., and W. E. Piller (2003), Possible refugia for reefs in times of environmental stress, *Int. J. Earth Sci.*, *92*, 520–531.

Rochford, D. J. (1991), 'Upwelling': Does it need a stricter definition?, *Aust. J. Mar. Freshwater Res.*, *42*(1), 45–46.

Rosenfeld, L. (1983), CODE-1: Moored array and large-scale data report, *Tech. Rep. 83-23*, 186 pp., Woods Hole Oceanogr. Inst., Woods Hole, Mass.

Schaeffer, A., M. Roughan, and B. D. Morris (2013), Cross-shelf dynamics in a western boundary current regime: Implications for upwelling, *J. Phys. Oceanogr.*, *43*(5), 1042–1059.

Schiller, A., K. R. Ridgway, C. R. Steinberg, and P. R. Oke (2009), Dynamics of three anomalous SST events in the Coral Sea, *Geophys. Res. Lett.*, *36*, L06606, doi:10.1029/2008GL036997.

Schiller, A., M. Herzfeld, R. Brinkman, and G. Stuart (2014), Monitoring, predicting, and managing one of the seven natural wonders of the world, *Bull. Am. Meteorol. Soc.*, *95*, 23–30, doi:10.1175/BAMS-D-12-00202.1.

Schiller, A., M. Herzfeld, R. Brinkman, F. Rizwi, and J. Andrewartha (2015), Cross-shelf exchanges between the Coral Sea and the Great Barrier Reef lagoon determined from a regional-scale numerical model, *Cont. Shelf Res.*, *109*, 150–163.

Sciremammano, F., Jr. (1979), A suggestion for the presentation of correlations and their significance levels, *J. Phys. Oceanogr.*, *9*, 1273–1276.

Shearman, R. K., and S. J. Lentz (2003), Dynamics of mean and subtidal flow on the New England shelf, *J. Geophys. Res.*, *108*(C8), 3281, doi:10.1029/2002JC001417.

Steinberg, C. (2007), Chapter 3 impacts of climate change on the physical oceanography of the Great Barrier Reef, in *Climate Change and the Great Barrier Reef*, edited by J. E. Johnson and P. A. Marshall, Great Barrier Reef Mar. Park Auth. and Aust. Greenhouse Off., Australia.

Warner, J.C., W. R. Geyer, and J. A. Lerczak (2005), Numerical modeling of an estuary: A comprehensive skill assessment, *J. Geophys. Res.*, *110*, C05001, doi:10.1029/2004JC002691.

Wolanski, E. (1994), *Physical Oceanographic Processes of the Great Barrier Reef*, CRC Press, Mar. Sci. Ser., Boca Raton, Fla.

Wolanski, E., and G. L. Pickard (1983), Upwelling by internal tides and Kelvin waves at the continental shelf break on the Great Barrier Reef, *Aust. J. Mar. Freshwater Res.*, *34*, 65–80.

Willmott, C. J. (1981), On the validation of models, *Phys. Geogr.*, *2*, 184–194.